OPEN ACCESS
IOP Publishing
Journal of Physics: Condensed Matter
J. Phys.: Condens. Matter **34** (2022) 333002 (33pp)
https://doi.org/10.1088/1361-648X/ac75a1

Topical Review

Surface nanopatterning by ion beam irradiation: compositional effects

L Vázquez[1,*], A Redondo-Cubero[2,3], K Lorenz[4,5], F J Palomares[1] and R Cuerno[6]

[1] Instituto de Ciencia de Materiales de Madrid (ICMM), CSIC, C/Sor Juana Inés de la Cruz 3, 28049 Madrid, Spain
[2] Grupo de Electrónica y Semiconductores, Departamento de Física Aplicada, Universidad Autónoma de Madrid, 28049 Madrid, Spain
[3] Centro de Micro-Análisis de Materiales, Universidad Autónoma de Madrid, C/Faraday 2, 28049 Madrid, Spain
[4] Instituto Superior Técnico, Universidade de Lisboa, Campus Tecnológico e Nuclear, Estrada Nacional 10, km 139.7, 2695-066 Bobadela LRS, Portugal
[5] Instituto de Engenharia de Sistemas e Computadores—Microsistemas e Nanotecnologia (INESC—MN), Rua Alves Redol 9, 1000-029 Lisboa, Portugal
[6] Departamento de Matemáticas and Grupo Interdisciplinar de Sistemas Complejos (GISC), Universidad Carlos III de Madrid, E-28911 Leganés, Spain

E-mail: lvb@icmm.csic.es

Received 16 March 2022, revised 13 May 2022
Accepted for publication 1 June 2022
Published 20 June 2022

Abstract

Surface nanopatterning induced by ion beam irradiation (IBI) has emerged as an effective nanostructuring technique since it induces patterns on large areas of a wide variety of materials, in short time, and at low cost. Nowadays, two main subfields can be distinguished within IBI nanopatterning depending on the irrelevant or relevant role played by the surface composition. In this review, we give an up-dated account of the progress reached when surface composition plays a relevant role, with a main focus on IBI surface patterning with simultaneous co-deposition of foreign atoms. In addition, we also review the advances in IBI of compound surfaces as well as IBI systems where the ion employed is not a noble gas species. In particular, for the IBI with concurrent metal co-deposition, we detail the chronological evolution of these studies because it helps us to clarify some contradictory early reports. We describe the main patterns obtained with this technique as a function of the foreign atom deposition pathway, also focusing in those systematic studies that have contributed to identify the main mechanisms leading to the surface pattern formation and development. Likewise, we explain the main theoretical models aimed at describing these nanopattern formation processes. Finally, we address two main special features of the patterns induced by this technique, namely, the enhanced pattern ordering and the possibility to produce both morphological and chemical patterns.

* Author to whom any correspondence should be addressed.

Keywords: surface nanopatterning, ion beam sputtering, chemical effects, co-deposition, ripple, dot, silicides

(Some figures may appear in colour only in the online journal)

1. Introduction

The research on surface nanopatterning by ion beam irradiation (IBI) has been attracting an increasing interest since the beginning of this century. Thus, many research groups have addressed the fundamental as well as the experimental and applied issues of this technique. IBI patterning was first reported in the sixties of the past century [1, 2]. Already in 1974 Taniguchi highlighted the potential and interest of the technique by its capacity to nanostructure the surface of several materials [3]. Nowadays, this prediction has been largely fulfilled, although it took 25 years to prove it [4–7]. Such a delay was partially due to the lack of adequate techniques to assess the morphological nanopatterning induced on the irradiated surfaces. The advent of the scanning probe microscopies, among other advances in surface characterization, filled in this gap and certainly contributed to enable the development of IBI induced surface patterning.

Today, substantial advances have been achieved both in the understanding of the mechanisms involved in IBI nanopatterning as well as in its experimental aspects. Thus, IBI has been successfully applied to induce patterns on a wide range of materials. Among them, we can mention: metals [4, 8], semiconductors [9–16], oxides [17, 18] ionic crystals [19, 20], and polymers [21–23]. In addition to this versatility, among the main attributes of IBI nanopatterning, we can also mention the large area that can be patterned, the short processing times and, finally, its cost-effective production. Thus, the technique has been applied in the last years in numerous fields such as magnetism [24–28], plasmonics [29], nanoelectronics [30], photovoltaics [31, 32], biomaterials [33], and sensing [34–37].

In the theoretical field, several approaches have been developed with different perspectives [5, 6, 38–40]. Chronologically, these advances started with Sigmund's seminal works [41, 42]. In these works, Sigmund realized that when a surface is bombarded at local oblique incidence, the local sputtering yield (SY) on top of a ridge is reduced whereas it becomes increased at the bottom of a valley. This scenario would turn a flat surface unstable upon ion bombardment. Later on, Bradley and Harper (BH) established the theoretical framework for IBI patterning when they showed that the pattern arises from the competition of this destabilizing ion-induced effect and the stabilizing one related to surface mass transportation [43]. Afterwards, many further improvements have taken place in the theory. Thus, additional physical mechanisms have been incorporated such as the non-linear dependence of the erosion rate on the local surface slope [44, 45], the ion-induced mass redistribution [46], surface viscous flow [47], stress effects [48–50], ion implantation [51, 52], etc. However, despite the advances mentioned above, a full theoretical understanding of IBI nano-patterning has not been attained, yet. This issue is complicated since the experimental findings undoubtedly show that the patterning is not a universal process since it depends on the specific target/ion combination. Thus, the topic is still being studied by different groups, with different approaches, see e.g. [39, 49, 53, 54] and references therein.

Likewise, the experimental advances have also been important in the last years. The very same subject of this review comes into play because it has had an influence not only on the experimental progress of IBI patterning but also on the pace of the theoretical modelling. This fact will be explained in more detail in the next section where a chronological description of the experimental advances will be given.

More specifically, this review addresses the IBI patterning when compositional effects are present during the irradiation process. Most of the early theoretical modelling and experimental work concerned mono-elemental surface targets bombarded by a noble gas ion beam. In this case, the inert ions become implanted to finally evaporate as the irradiation proceeds. However, as it will be shown in section 2, other systems were studied where this compositional homogeneity did not occur, in many cases inadvertently. The compositional effects arise when the irradiated surface is, or becomes, during the IBI process heterogeneous in terms of composition, i.e. is formed by different atomic species. Accordingly, as it will be shown in sections 3–5 this fact can lead to local differences in processes such as SY, surface diffusivity, etc than indeed influence the surface patterning. Therefore, at this stage, it is necessary to define the two basic IBI systems depending on the presence or not of compositional effects:

(a) Noble gas IBI of mono-elemental surfaces where compositional effects do not operate. A further classification can be established based on the irradiated surface: (i) those that remain crystalline upon ion bombardment, such as metals, in which Ehrlich-Schwoebel barriers can have an important role on the patterning process [4]. A particular context that should be mentioned here is that of radiation resistant materials. Some materials, despite their multi-elemental character, such as ZnO, GaN, SiC, or CdTe exhibit a strong dynamic annealing that leads to saturation of defect levels, even at low temperatures [55, 56]. As a result, the formation of patterns in these crystals does not necessarily follow the conventional mechanisms, although they can, in certain situations, produce ripples [18, 57]; (ii) surfaces that are amorphized by the incoming ions, such as mono-elemental semiconductors (Si, Ge); (iii) those that are fully amorphous, such as polymers and glasses. We include them in this type because, to the best of our knowledge, there is not any report on compositional effects in IBI experiments on these materials.
(b) IBI patterning experiments where compositional effects operate. We can distinguish the following cases:

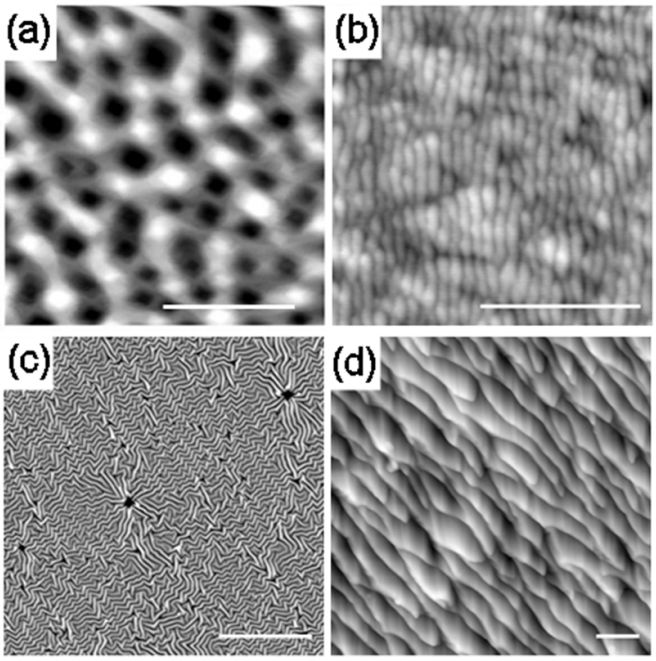

Figure 1. STM (a) and AFM (b)–(d) images of surface patterns induced by IBI on different materials: (a) Ag (001) under 1 keV Ar^+ irradiation at normal incidence. Reproduced from [4]. (b) Si under 1 keV Ar^+ irradiation at $\theta = 65°$; (c) PDMS under 1 keV Ar^+ irradiation at $\theta = 20°$; (d) ZnO under 20 keV Ar^+ irradiation at $\theta = 60°$. The horizontal bars correspond to 50 nm (a), 500 nm (b), (d), and 10 μm (c), respectively.

(i) noble-gas IBI of compound semiconductor targets (GaSb, InP, etc) where preferential sputtering of one of the elements can take place; (ii) IBI with concurrent metal co-deposition. In this case, IBI usually takes place using a noble gas ion beam impinging on a mono-elemental semiconductor (Si) while metal atoms, such as Fe or Mo, are concurrently and externally supplied on the target surface. Usually, the metal atoms react with the target ones forming a silicide. This is the main focus of this review; (iii) a special case is that where a non-noble gas ion beam bombards the surface, usually a mono-elemental semiconductor, and as the ions are incorporated on the target surface, the latter becomes compositionally heterogeneous, which leads to the appearance of compositional effects.

Examples of the patterns induced by IBI under different incident angles, θ, on the surface of different materials are displayed in figure 1, where images obtained by scanning tunnelling microscopy (STM) and atomic force microscopy (AFM) are shown.

As already noted, the main focus of the review refers to IBI with concurrent metal co-deposition. The production of these patterns was reported in the wake of the general interest triggered by the seminal work by Facsko *et al* [9]. However, at these initial stages, the existence of the impurity supply remained unnoticed and all the experimental reports were then attempted to be understood within the theoretical framework employed for impurity-free patterning of mono-elemental surfaces. To add more confusion, the experimental reports were strongly dependent on the specific set-ups employed. These facts turned the understanding of IBI patterning into a puzzle both from the experimental and the theoretical perspectives. It took about 10 more years to clarify the state of the art of the technique. For this reason, we include in this review many of the works published before 2009–2010, including publications by some of the present authors, which reported patterns that today are understood as induced by the impurity co-deposition process, although the authors were not aware of it at the publication time. Also, we want to note that the main part of the experimental works cited in the review deals with silicon targets and metal (usually Fe or Mo) co-deposition. This is the case because most of the works were focused on this configuration, mainly because silicon is a flat, affordable, and technologically relevant material [6].

Due to the gradual awareness of the complexity of IBI patterning just mentioned, it is convenient to give a chronological account of how the community became aware of the different problems present in the different reports and then was able to establish the correct understanding. We find this description useful also because it allows us to rationalize the reports that appeared in this initial decade from today's perspective.

2. Chronological perspective

Although reports were available in the nineties of the past century on IBI-induced surface rippling for different targets such as Si [46], Ge [58], GaAs [59, 60], InP [59, 61], and SiO_2 [62], it was the report in 1999 by Facsko *et al* [9] on highly ordered nanodot patterning of GaSb surfaces which triggered an extensive and intensive research on IBI patterning during the next two decades. This interest was indeed aroused by the capability to produce semiconductor quantum dots cost-effectively and rapidly. Several target materials were irradiated in order to produce hexagonal nanodot patterns like those obtained on GaSb. Two of the present authors participated in the first report in 2001 of nanodot patterns on silicon surfaces [63]. These patterns displayed a poorer order than those produced on GaSb as figure 2 shows.

Due to the technological relevance of Si nanodots, from this moment on, several groups performed experiments to reproduce and further investigate them [64–68], as well as to produce them in other materials such as MgO [69]. These studies resulted into a rather confusing scenario as some groups were unable to reproduce the results, others did, but at different irradiation conditions (noticeably at different incident angles) and, when the nanodots were obtained, often they displayed different degrees of order. We can summarize the situation quoting Cuenat and Aziz: '*(Our) features are qualitatively different from those reported by Gago et al under the same conditions and we cannot reproduce their results. Also, the features are not nearly as regular as the "quantum dots" produced by Facsko et al on GaSb. The underlying reasons remain a puzzle*' [64].

The different experimental results seemed to depend, to some extent, on the specific experimental set-up. In fact, some

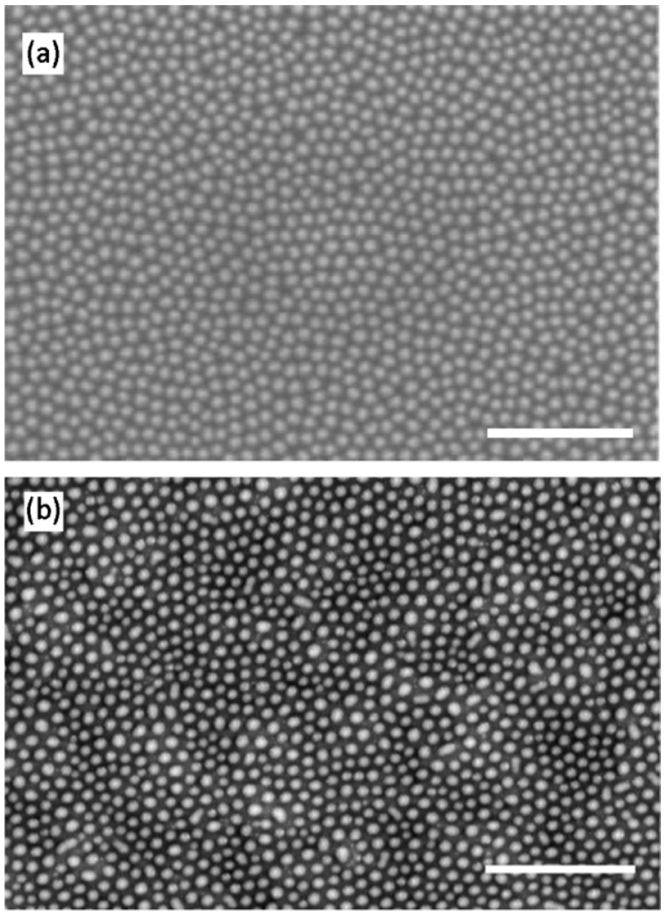

Figure 2. Typical dot patterns induced by IBI under normal incidence conditions on: (a) GaSb, imaged by scanning electron microscopy (SEM). From [9]. Reprinted with permission from AAAS; (b) Si with metal (Fe) co-deposition (AFM image). The bars indicate 500 nm.

groups pointed out that the ion gun irradiation conditions were important [70]. This puzzle affected not only the experimentalists, but also the theoreticians who aimed at understanding the mechanisms leading to these interesting nanodot patterns [71–78]. It should be noted that at this stage, the compositional effects did not play any role in the theoretical modelling. More experiments were designed and carried out. From their results, an awareness that the unnoticed supply of impurities (i.e. contamination) during the IBI process could be the origin of some of the nanodot patterns (mainly those on silicon) started to emerge [79, 80]. This simultaneous impurity supply was suggested to come from the bombardment of metal parts of the sample holder, as well as from different elements of the vacuum chamber that were eventually hit by the broad ion beam. This is the reason why most of the works cited in this review employ metals as co-deposited species. This line of thought could explain the variability of the experimental reports.

Then, in 2008 Madi *et al* published insightful reports addressing this issue experimentally [81, 82]. In these works, Madi *et al* shielded with silicon pieces all places inside the irradiation chamber prone to be hit by the argon ion beam. Under these conditions, they irradiated a silicon target at different angles. In this way, they established that, under impurity-free conditions, the silicon surface was ripple patterned only for θ values above a threshold angle close to 50°. Below this threshold angle the surface remained flat and featureless, in agreement with the earlier findings of Ozaydin *et al* [79]. Moreover, this observation agreed qualitatively with the theoretical argument by Carter and Vishnyakov (CV) [46] that at low incidence angles ion induced surface relaxation dominates and, consequently, no patterns are formed.

The effect of uncontrolled impurity deposition is consistent with the reported difficulty to reproduce the experimental results in different laboratories, since its supply pathway depends on the particular experimental set-up. In this sense, it is worth to mention the possibility that the ion beam is not pure, i.e. it contains impurities, as Bhowmick *et al* studied much more recently [83].

After the results of Madi *et al*, further works confirmed the essential role played by (un)intentional metal supply in the development of patterns, under experimental conditions in which they were not expected [84–88]. Once the IBI patterning scenario was clarified, two different branches can be distinguished in later research: (i) studies dedicated to analyse and understand, both experimentally and theoretically, IBI patterning of surfaces under 'clean' conditions, i.e. without any impurity supply; (ii) studies of IBI systems where the metal supply was present and mainly intentional.

The first branch is the one that has been more extensively studied not only experimentally but also theoretically. This is so because the presence of metal impurities may add different new mechanisms that complicate the modelling and understanding of the process. Most of the experimental work has been focused on mono-elemental surfaces, such as Si and Ge, also for the sake of simplicity. There have been many studies and reviews devoted to this issue that can be consulted in the literature [5, 6, 40, 89]. However, despite all the efforts devoted to understanding this process that have led to important advances, a consensus has not yet been reached from the theoretical point of view about the fundamental driving mechanisms as different proposals are still being made, see e.g. [39, 49, 54] and references therein.

In contrast, the branch of studies devoted to surface patterning via IBI with concurrent impurity co-deposition has received less attention. This can be due to the relative disparity in the early experimental reports, mostly dependent on the specific experimental set-ups. Starting with the initial works by Höfsass and Zhang [90] and Macko *et al* [85], specific experimental configurations were designed that allowed for a more systematic study of the characteristic features of this patterning technique, which were then adopted by other groups. The ensuing advances also allowed to develop theoretical models addressing the particularities of the technique. These works studied the relevance of the main variables that are involved in IBI surface patterning, namely ion energy and species, ion beam incidence angle, ion flux, ion fluence, target temperature, and set-up geometry. In the following, we summarize the current understanding of the main mechanisms governing this type of IBI patterning in order to provide the readers with some background that enables understanding the different

issues addressed in the reports presented along the present work.

As already noted in the Introduction, IBI patterning without compositional effects is still the subject of theoretical research through different approaches. What it is clear, and applicable to most of the systems shown in this review, is the key role played by the ion induced amorphization of the outmost surface layer. The ion impacts produce a series of craters and collision cascades [39] that lead to the surface amorphization as it occurs for semiconductor targets [91]. This process induces residual stress that is relaxed via surface confined viscous flow [11, 47–49]. This mechanism can be stabilizing or destabilizing [46], depending on factors such as ion/target species, ion energy and ion angle of incidence [92, 93]. In general, a low incidence angle stabilizes the surface and hampers pattern formation. Thus, the IBI induced amorphous layer plays an important role in the patterning process, via its free interface [47–49] and/or its amorphous to crystalline (a/c) interface [50, 92, 94–97]. Therefore, under these conditions, the Erlich-Schwoebel barriers to surface-diffusion induced by the crystalline structure do not play any role, unless IBI takes place at target temperatures above the surface recrystallization temperature [98–100]. In addition, other mechanisms are also present such as ion implantation [52] and surface sputtering [53, 101], whose relative importance also depends on physical parameters like the ion angle of incidence and other [102].

All these processes also operate in the systems discussed in this review. However, it is evident that additional mechanisms must be at work when the target surface has, or develops, a compositional heterogeneity because patterns are produced under irradiation conditions for which they are not produced on mono-elemental surfaces (i.e. at low ion incidence angles). As highlighted by Shenoy *et al* [103], the different surface diffusivities of the different elements as well as their different SY are key to inducing a surface pattern. This also holds when a new compound is formed, as in the case of silicide formation for concurrent co-deposition systems. Particularly, the different SY of the surface elements or compounds causes preferential sputtering where the regions rich in the element with lower SY protrude while the surrounding areas, rich in the element with higher SY, are eroded more efficiently. In the case when the element associated to the lower SY is supplied externally and concurrently with IBI (as in the co-deposited systems and those where the ion beam itself provides this external element) the directionality of this external flux plays an important role as will be shown in section 3. In these cases, there is a synergy between the development of surface morphological fluctuations caused by the ion irradiation and the formation of low sputtering compounds (e.g. silicides) as shown by Engler *et al* and Bradley [13, 104]. This explains why the IBI geometry becomes so important in these systems. Thus, the preferential sputtering effects caused by the surface heterogeneity triggers the pattern development, although the contribution of stress effects associated to the ripple or dot formation can also be important [105].

Although the role of compositional effects in IBI patterning has been considered in some previous reviews, there is a lack of a specific journal review on the subject. The aim of the present manuscript is to fill in this gap and review the current state of the art of IBI surface patterning when compositional effects also operate. As already noted, the main focus will be addressed to IBI in the presence of impurities.

We will consider both experimental results and theoretical models. We are aware that different options are valid to describe them but, according to the aim of the review described in its title and abstract, we have chosen to present them in section 3 as a function of the source of heterogeneity: (i) noble gas IBI with metal concurrent co-deposition, (ii) non noble gas IBI, and (iii) IBI of compound targets. With these examples, we hope the reader can obtain an overview of the different patterns and dependences that can occur. In section 4 we will focus on experimental studies on concrete mechanisms that can operate in the pattern formation and development as well as on the role played by experimental parameters such as target temperature and ion energy and species. Later on, section 5 is devoted to the main theoretical models addressing the patterning of surfaces under the conditions considered in this review. Section 6 will show special features of IBI patterning when compositional effects are present, to finally summarize the main conclusions.

3. Phenomenology of the pattern dependence on the source of compositional heterogeneity

Before describing the main experimental reports, it is worth giving details on the different parametrizations of the induced patterns. This will contribute to their better understanding. Among the main parameters describing the pattern morphology are the surface roughness, σ, and the pattern wavelength, λ. The latter is the basic periodicity of the ripple or dot pattern. It is usually obtained through the power spectral density (PSD) of the surface morphology [6]. Namely, if the pattern is clear and displays some degree of in-plane ordering, the wavelength can be obtained from the wave vector ($k = 1/\lambda$) at which the PSD vs. k plot shows its main peak. If the pattern is quite ordered the width of this peak is small and additional (harmonic) peaks appear at larger k values. These two features, peak width and number of harmonics, are frequently used as a measure of pattern ordering. Furthermore, the pattern ordering can be also evaluated following different procedures for the ripple [106–108] and dot patterns, e.g. the latter by Voronoi tessellation [109, 110]. In this sense, the fast Fourier transform (FFT) as well as the auto-correlation function (ACF) of the microscopy images of the irradiated surfaces are very helpful to characterize the pattern ordering.

In many reports, the dynamics of the pattern formation and development is studied. This is usually done by real-time techniques such as grazing-incidence small-angle x-ray scattering (GISAXS) and even STM, or *ex-situ* ones like AFM. From these data the increase of the surface roughness (roughening) and wavelength (coarsening) with the ion fluence (i.e. time, t) can be obtained. For cases in which the surface morphologies show substantial fluctuations, these dependences are usually contrasted with the predictions of the different continuum models (see below) using the concepts of the dynamic scaling

theory [111], which describes the surface morphology evolution of so-called kinetically rough surfaces through three critical exponents. Thus, the surface roughness, σ, evolves with time, t, as $\sigma \propto t^{\beta}$ where β is known as the growth exponent. Likewise, the lateral correlations of the surface roughness are obtained from the following relationship: PSD $\propto k^{-(d+2\alpha)}$, where $k = 1/l$, l being length in real space, and α is called the roughness exponent, which is related with the fractal dimension of the surface. Here, d is the Euclidean dimension of the target. It is usually 2 but, for instance, $d = 1$ is to be used for analysing e.g. ripple patterns if the PSD is computed along the direction of the ripple wave vector only. Finally, there is a third exponent, termed as the coarsening exponent, $1/z$, which describes the increase of λ with time as $\lambda \propto t^{1/z}$. These three exponents are related and different models predict different values for them.

Once we have introduced the main parameters used to characterize the patterned surfaces, we present the main experimental works devoted to pattern formation on compositional heterogeneous target surfaces. We have based this description on the source of the chemical heterogeneity. Thus, the first subsection refers to mono-elemental targets (silicon) under noble gas irradiation with either anisotropic or isotropic metal co-deposition. The next subsection refers to patterns produced with non-noble gases ion species, which can be either reactive (i.e. forming compounds during the irradiation) or non-reactive (no chemical interaction with the surface is expected). Finally, we also consider the irradiation of compound substrates, which can exhibit much complex behaviours.

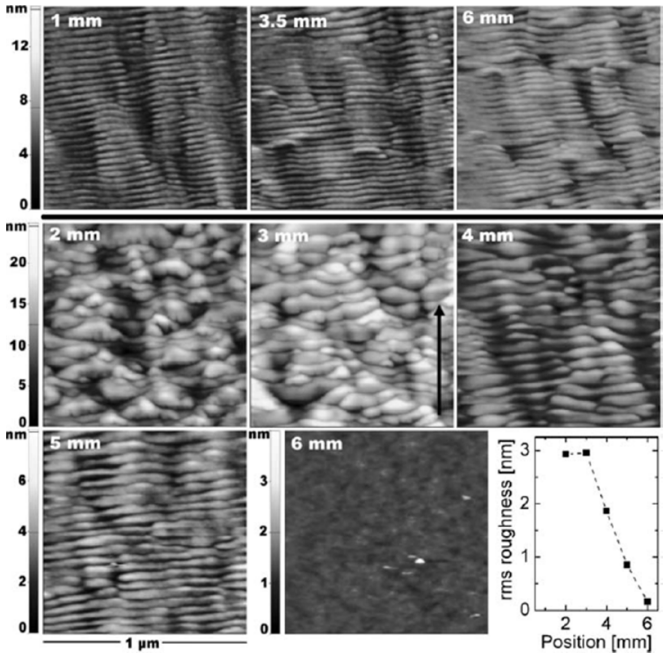

Figure 3. AFM images of a Si target irradiated by 10^{17} at cm^{-2} 5 keV Xe^{+} with $\theta = 70°$ with a simultaneous Si (top row) and Au foreign atoms (middle and bottom rows) flux. The arrow indicates the projected ion beam direction. The foreign atom flux comes from the opposite direction. The position indicated in each image indicates the closeness to the adjacent plate (in this case, a higher value implies a closer location). The plot at the bottom right corner shows the surface roughness vs. the distance. Reproduced from [90], with permission from Springer Nature.

3.1. Noble gas ion irradiation with metal co-deposition

3.1.1. Anisotropic metal supply. When the impurity flux is directional, mainly, but not only, ripple structures appear. The experimental set-up designed by Höfsass *et al* [90, 112] proved to be a key tool for studying this sort of patterning in a systematic way. This scheme is very similar to that displayed in figure 4(a). In this type of set-up both the silicon target and the tilted steel plate are simultaneously irradiated by the vertical ion beam. Thus, the sputtered atoms from the plate land on the bombarded silicon surface. With this configuration, it is not possible to control quantitatively the impurity flux. However, this flux decreases with the distance from the steel plate along the Si target. This fact was successfully used in several studies to characterize the patterns as a function of the (mainly Fe) impurity flux. This set-up was adopted in several studies with slight changes, such as a non-normal ion beam incidence angle, different tilt angles of the steel plate, etc.

Some of the most insightful systematic studies of the co-deposited IBI have been made using this experimental configuration. In the following we will describe their main results. The first work using this set-up was carried out by Hofsäss and Zhang [90]. The authors used either silicon itself or gold as co-deposited atoms on a silicon target irradiated by a Xe^{+} ion beam at an incidence angle above the threshold value. Figure 3 shows an example of the influence of the foreign atom nature on the final pattern.

The authors report that using Si as co-deposited atom does not affect the patterning (although it changes the effective SY). However, the incorporation of Au does change drastically the ripple morphology, particularly the wavelength and amplitude. Note that, as the ion beam incidence angle is high, a ripple pattern develops also when foreign atoms are not co-deposited. As the position is closer to the Au source, the Au content increases whereas the roughness decreases. For the closest position the pattern vanishes. In all cases, the ripple wave vector runs parallel to the projected direction of the ion beam. In this work, Hofsäss and Zhang coined the term 'surfactant sputtering' to describe this sort of IBI patterning with concurrent co-deposition of foreign atoms that would act as surface active agents [90].

Another important work using the same set-up was reported by Macko *et al* [85]. The main results are shown in figure 4. This configuration allows to characterize the morphologies induced as a function of the distance to the steel plate. With increasing distance the surface changes from flat with nanoholes to ripples with the wave vector parallel to the ion beam projected direction. For larger distances a combined ripple-dot pattern appears that turns into a dot one for even larger distances. Finally, for large enough distances the surface remains flat. Note in figure 4(h) the correlation between the Fe content and the pattern type. As the ejected Fe atom flux weakens its directionality with the distance, the morphology evolves from quite a directional ripple pattern to a poorly ordered dot

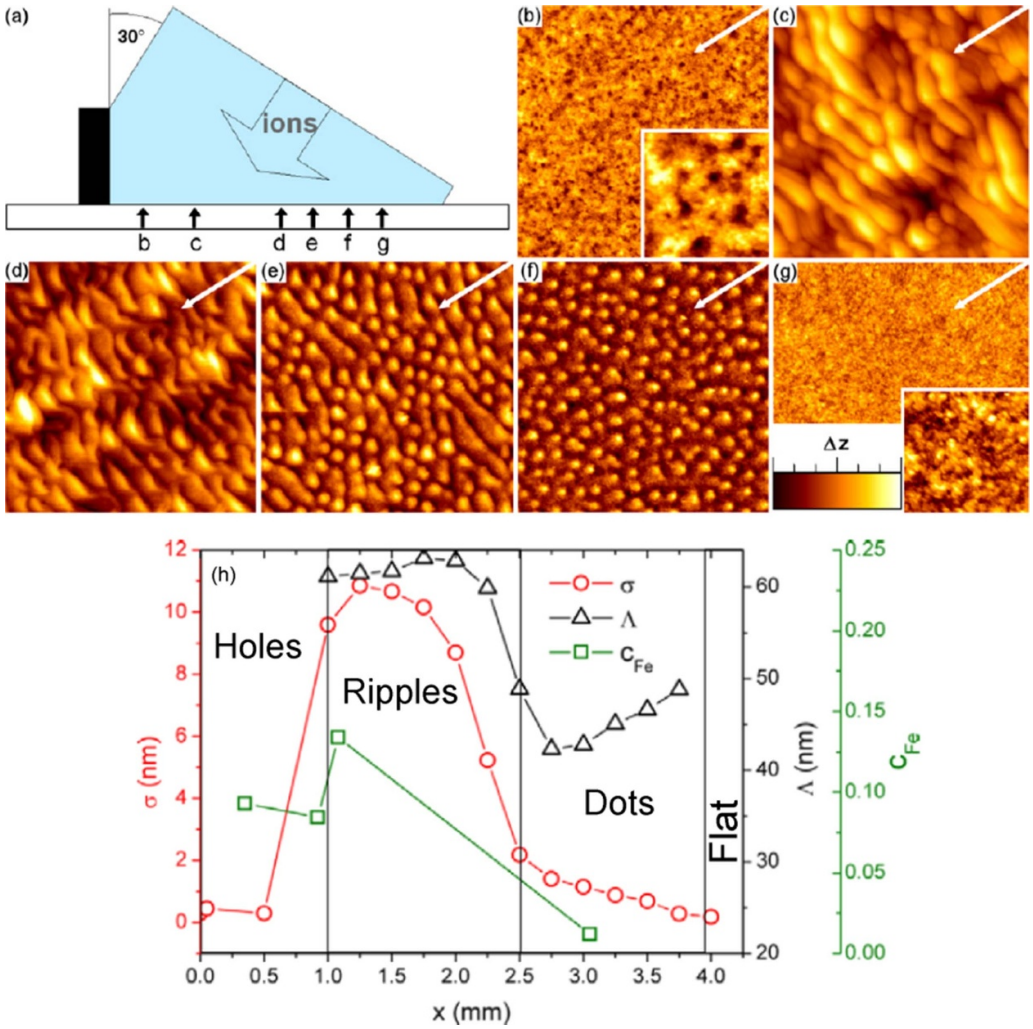

Figure 4. (a) Experimental set-up of the 2 keV Kr^+ irradiation experiments on Si (ion fluence close to 5×10^{17} ions cm^{-2}) with the steel plate at the left. The different positions in which the (b)–(g) STM images (625×625 nm^2) were taken are indicated. Insets in (b) and (g) are 100 nm wide. The ion beam direction is marked with white arrows. (h) Plots of roughness, wavelength, and Fe content as a function of the distance to the stainless steel plate, where four morphological regions are indicated and separated by vertical lines. Reproduced from [85].

arrangement, which is rather characteristic of a non-directional incoming Fe flux at long distances (see below).

In this work an important feature of the ripple patterns produced by IBI with co-deposition was demonstrated. The ripple wave vector is not, in fact, oriented along the projected ion beam direction but rather along the direction of the incoming Fe (or impurity) flux. This is nicely shown in figure 5 where it is evident that the ripple wave vector depends on the position with respect to the metal source.

The same group designed [113] a nice next experiment to validate this finding. In most of the experiments shown in this review, the impurity flux is coupled to the ion flux beam since the metal is sputtered from the adjacent metal plate. This hinders control not only on the metal flux but also on the relative angle between both fluxes, since, with the set-up shown in figure 4, they follow opposite directions. Macko *et al* uncoupled these two fluxes by evaporating the metal on the target surface simultaneously to the IBI. They assayed different geometrical configurations (see figure 6) and obtained a pattern on the target surface only when the angle between the two fluxes was large enough. This finding also accounts for the conflicting previous reports on pattern formation.

The above results were obtained for fixed ion fluence conditions. In a later work, Zhang *et al* [112] addressed the pattern evolution with the ion fluence for a constant Fe content. It was found that, for each distance to the impurity source, the Fe content attained a steady-state value after a given ion fluence, i.e. equilibrium is reached on the target between the metal sputtering and metal deposition processes. Under this condition, the pattern evolution was studied during subsequent ion bombardment. Noticeably, it was found that for high enough Fe content the pattern evolved with ion fluence from a weak mixed dot-ripple morphology to an unambiguous ripple one, in which the ripples increased their length and amplitude and the pattern became more regular. This feature will be discussed in more detail in section 6, as it is a fingerprint of this sort of IBI patterning. This behaviour was later confirmed by the same group for other metals, such as W, Mo, Ni, and Pt, the latter

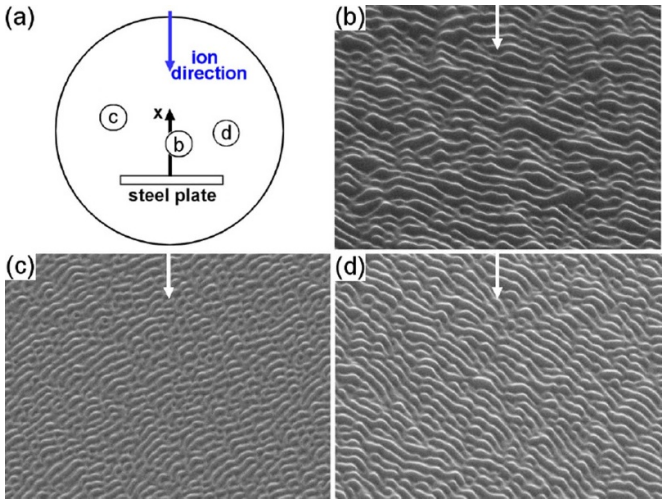

Figure 5. (a) Scheme of the experimental set-up indicating the zones (b)–(d) where the corresponding SEM images were taken. Same irradiation conditions as in the previous figure were employed. Reproduced from [85]. © IOP Publishing Ltd. All rights reserved.

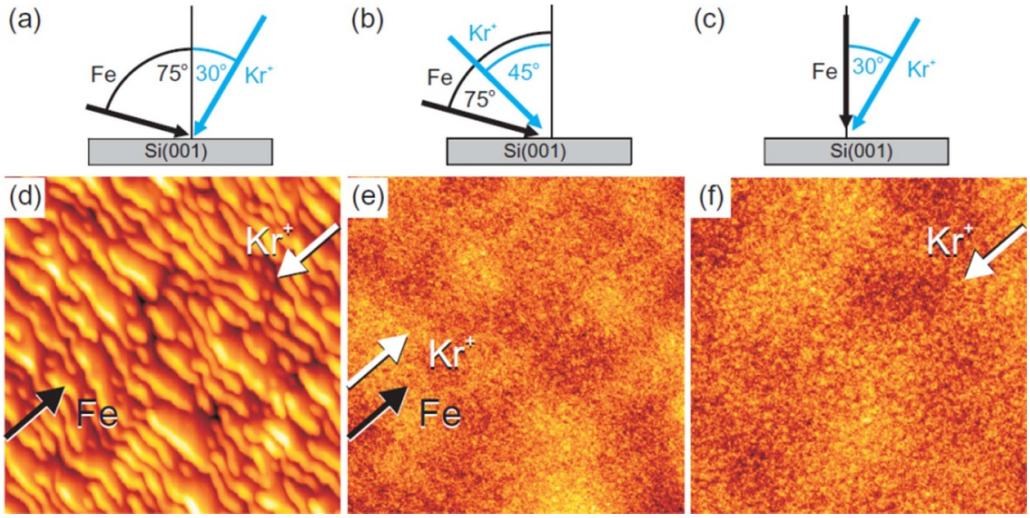

Figure 6. Dependence of the pattern formation on the relative directions of the incoming metal flux and 2 keV Kr^+ ion beam as sketched in (a)–(c). Below (d)–(f) are displayed the corresponding AFM images of the irradiated surface. Reproduced from [113]. © IOP Publishing Ltd. CC BY 3.0.

displaying a slightly different dependence as no dot pattern was observed [114]. In particular, when Mo was used as co-deposited species, the transition from a flat morphology to a ripple pattern was found to occur faster and at lower ion fluences when the metal content was higher. In contrast, for less Fe content the flat surface evolves into a dotted pattern, for which the dot height increased with ion fluence. From this study, a pattern sequential evolution: (i) flat, (ii) dot, (iii) mixed ripple-dot, (iv) ripple, was obtained as the steady-state Fe content increased, in agreement with the work by Macko *et al* [85].

These dependences are summarized in figure 7, which includes the pattern distribution as a function of experimental variables such as the distance to the metal source, temperature, and Fe steady-state coverage, taken from both reports. It is worth noting that Macko *et al* [113] did not find any clear effect on the pattern morphologies for temperatures in the 140–440 K range. It should be stressed that the metal content decreases with the distance to the plate. These trends were confirmed by different groups using similar set-ups [115, 116]. In particular, the transition from dot to hole nanopatterns for increasing metal content had been also reported for other set-ups by Sánchez-García *et al* [117].

An additional morphological feature appears with this set-up for a narrow range of small distances to the metal plate, close to the transition between flat/nanohole and ripple morphologies. This feature was termed as 'bug'; some examples are shown in figures 8(a)–(d), where AFM, SEM and magnetic force microscopy (MFM) data are displayed.

Similar structures were also found by Zhang *et al* [115]. As the images show, the bugs are isolated structures with a three-dimensional profile that reaches its maximum at the location closest to the incoming ion beam. The structure is composed by a series of parallel ridges whose wave vector runs parallel to the projected ion beam direction.

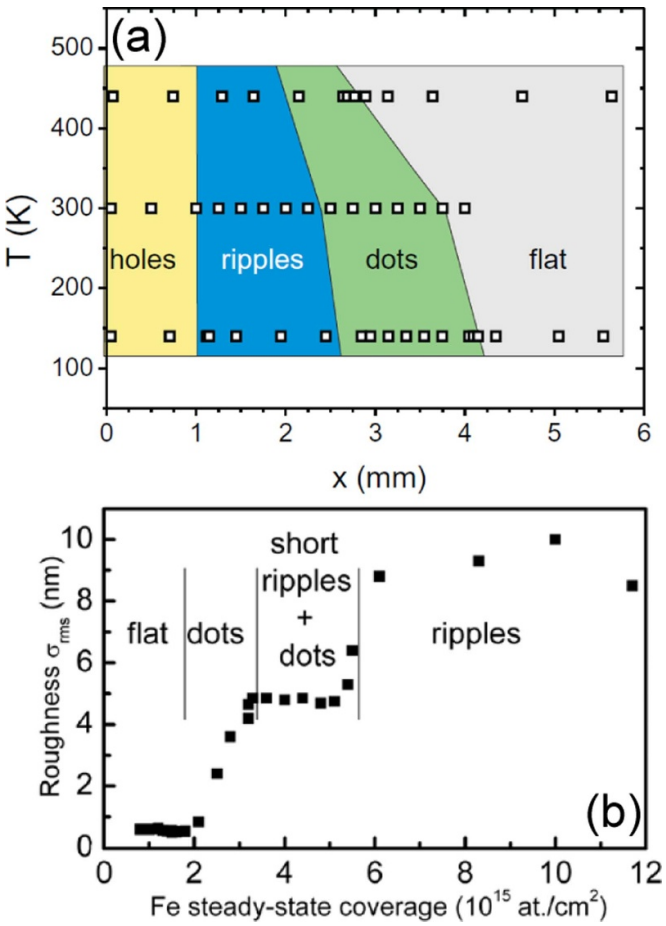

Figure 7. (a) Pattern-type map as a function of the distance to the stainless steel and temperature. Reproduced from [113]. © IOP Publishing Ltd. CC BY 3.0. (b) Pattern evolution and surface roughness as a function of the Fe steady-state coverage. Reproduced from [112]. © IOP Publishing Ltd. CC BY 3.0.

Interestingly, similar structures were produced when a silicon target was irradiated by a 40 keV Fe^+ ion beam at $\theta = 40°$ [109]. Some examples are shown in figures 8(c) and (d). Here, the ridges have a more marked fan-like curvature but, still, their wave vector runs parallel to the ion beam direction and, remarkably, also parallel to the ripples formed on the background surface. Finally, figure 8(d) shows superimposed the topographical and force magnetic signals indicating that the top of the ridges are Fe-rich. The existence of these bugs does not seem to be an anomaly since they have been reported thrice and with quite different set-ups, although it is true that they are produced on a rather confined area of the target.

Both research groups [112, 113], reported almost simultaneously a key aspect of this type of ripple patterning, namely the preferential concentration of the co-deposited material on the side of the ripple facing the incoming Fe flux. Both studies were carried out at room temperature. This is shown in figure 9, which shows transmission electron microscopy (TEM) and electron energy loss spectroscopy (EELS) analysis of the ripples formed on Si by a 2 keV Kr^+ ion beam impinging at $\theta = 30°$. In these images the bright zones corresponding to the Si amorphized by the beam are visible. The darker zones on the ripples facing the Fe flux are Fe(Cr)-rich, as shown in the corresponding EELS spectra shown in (c) and (d).

In a further study, Macko *et al* studied the same process but at a higher target temperature of 660 K, at which the silicon sample remains crystalline [118]. They used the same set-up and reported quite different induced morphologies. As figure 10 shows, now rather than nanoripples or nanodot structures, nanopillars emerge with different sizes and tilt angles depending on the position on the target surface. Their tips are Fe-rich as the TEM and energy dispersive x-ray (EDX) spectroscopy data show. X-ray diffraction data revealed the presence of FeSi structures on the pillars of figures 10(a) and (b).

The scheme of figure 11 summarizes the main structures produced on the Si target with the stainless steel plate set-up for two temperature conditions as a function of the distance to the plate. It is worth noting that the sample bombarded at 440 K is similar to that irradiated at room temperature, see figure 7.

These differences were understood in terms of the balance between the ion-induced and the thermal mobilities. When the former is prevalent (lower temperatures) the patterns do not depend on temperature (see figure 7(a)). However, when the thermal mobility is the dominant one, the pattern does depend on the temperature and structures with high aspect ratios develop since transport is enhanced along the vertical direction.

The examples shown in this section demonstrate how versatile the structures induced with this technique can be, once the different parameters and set-ups are properly tuned. Although these studies were performed on Si targets, a similar set-up led to similar conclusions for sapphire surfaces [119].

Finally, it is worth mentioning that similar behaviours were found when medium-energy ion beams were employed for the irradiations [108, 120], specifically for a 40 keV Ar^+ ion beam. In both works, a plate set-up, similar to those used above, was employed. However, the incidence angle conditions were different. In the first study, it was 60°, whereas in the second study, it was 15°. Thus, under the first condition a ripple pattern would be induced even without metal co-deposition, while in the second one, without this external supply, the surface would remain flat, which is a condition similar to those used by Zhang *et al* and Macko *et al* [85, 90, 112, 113]. The former condition has been scarcely considered, while it allows for the comparison with ripple patterning without compositional effects.

Figure 12 shows characteristic AFM images of the patterns induced on the silicon surface by IBI with metal (Fe) co-deposition for two ion fluence values. The incidence angle is the only difference in the experimental set-up, which causes that the SY on the Fe plate is also different. Thus, the steady-state Fe coverage results to be four times larger for the $\theta = 60°$ set-up than in the 15° case. When $\theta = 60°$, a well-defined ripple pattern develops that becomes rather rough and disordered upon sustained irradiation. In contrast, at $\theta = 15°$, an initial disordered dot pattern evolves towards parallel rows of dots. This pattern evolves under further irradiation into a quite ordered ripple pattern [108]. Noticeably, the roughness of the pattern is rather stable and much lower than that

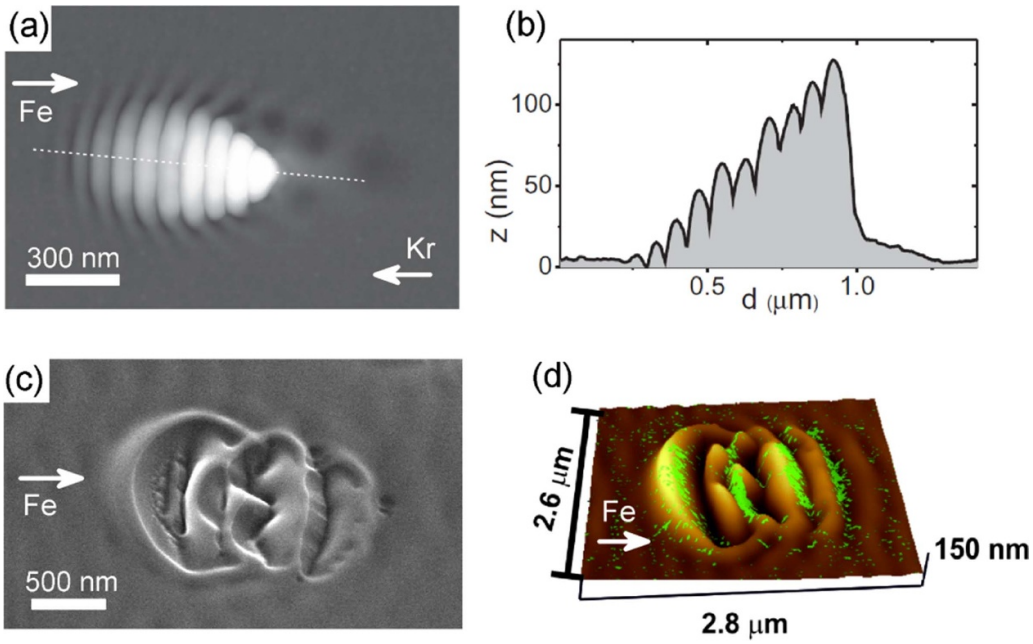

Figure 8. (a) AFM image of one bug measured approximately 1 mm away from the stainless steel plate in the experiment by Macko *et al* [113] using a 2 keV Kr^+ beam. (b) The height profile corresponding to the dashed line in (a). The arrows indicate the direction of the Fe and Kr^+ fluxes. (a), (b) Reproduced from [113]. © IOP Publishing Ltd. CC BY 3.0. (c) SEM image of one bug produced on a Si target irradiated with a 40 keV Fe^+ ion beam at $\theta = 40°$. (d) AFM image of one bug similar to that displayed in (c). The high MFM phase shift regions are superimposed in green. Reproduced from [109]. © IOP Publishing Ltd. All rights reserved.

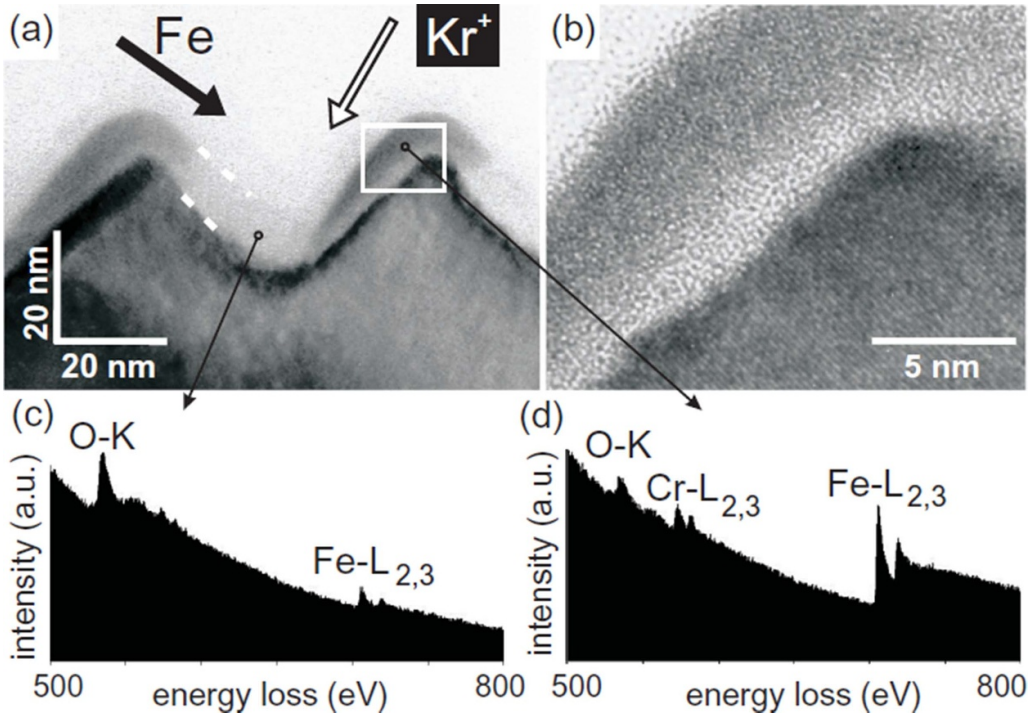

Figure 9. (a) Cross-sectional bright-field TEM images of ripples obtained by 2 keV Kr^+ IBI with Fe and Cr co-deposition. The dashed lines enclose the amorphized Si layer. Both, Fe and ion beam fluxes are indicated. (b) High-resolution image of the zone marked by the rectangle in (a). From the valley, and close to the ripple ridge, two arrows indicate those locations in which the EELS spectra shown in (c) and (d), respectively, were taken. Reproduced from [113]. © IOP Publishing Ltd. CC BY 3.0.

produced at $\theta = 60°$. In fact, despite the larger ion energy employed here, the pattern obtained at $\theta = 15°$ is quite similar to those described above for low-energy IBI. Now, the wavelength of the pattern is larger than those obtained at low energies because its magnitude scales with the ion energy [6].

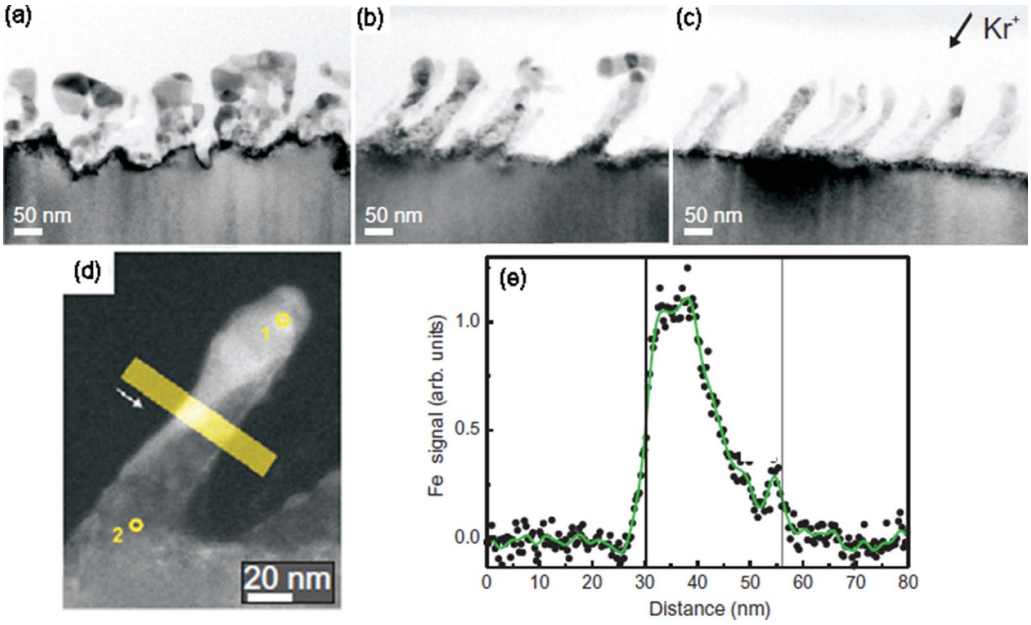

Figure 10. (a)–(c) Characteristic TEM images taken on the 2 keV Kr^+ irradiated Si surface at 660 K and at increasing distances from the stainless steel plate. (d) Energy-filtered TEM measurement of a nanopillar corresponding to zone (c) where bright regions represent Fe-rich content. (e) EDX line scan along the yellow line depicted in (d), where the vertical lines mark the border of the pillar. Reproduced from [118].

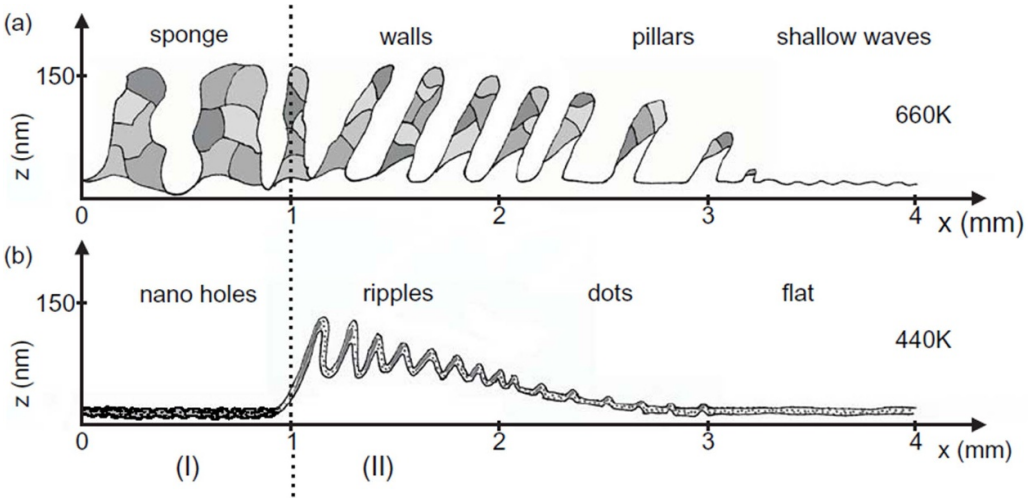

Figure 11. Scheme of the different morphologies produced by 2 keV Kr^+ ion sputtering with the stainless steel plate set-up at 660 K (a) and 440 K (b), as a function of the distance to the plate (i.e. for decreasing metal content). Reproduced from [118].

3.1.2. Isotropic metal supply. It has been shown above how nanodot structures can form on the target surface using the stainless steel plate configuration in which the Fe flux is anisotropic. This type of pattern usually is produced at large distances from the plate, when the Fe flux has likely lost much of its directionality, and for low Fe contents. Normally, these patterns are not stable and evolve into ripple ones upon further ion irradiation. In contrast, stable nanodot patterns are obtained when the metal flux is isotropic and the ion beam impinges under normal incidence on the target surface. As discussed above, initially this short-range hexagonally ordered nanodot silicon patterns attracted a lot of interest after the seminal work by Facsko *et al* on GaSb [9]. However, the dot patterns induced on silicon are not as compact, ordered, or close-packed as those produced on GaSb (see figure 2).

The most systematic, and controlled, way to induce a nanodot pattern on silicon consists in irradiating it at normal incidence using a mask with a circular hole at the centre, placed on top of the silicon target (see scheme in figure 13(a)). In this way Fe atoms are ejected from the mask and land isotropically on the centre of the target surface.

Figure 13(b) shows how the metal content in the irradiated surface, evaluated by XPS, increases from the perimeter to decrease slightly around the centre where it reaches a plateau

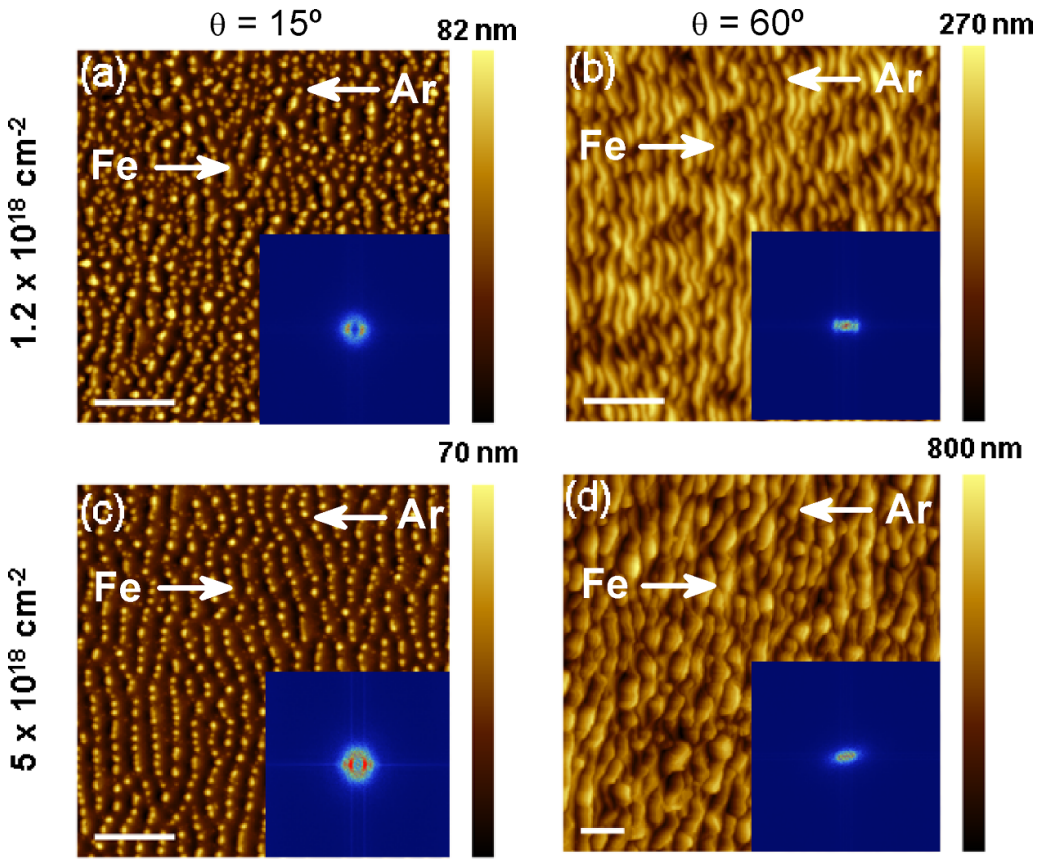

Figure 12. AFM images of the patterns induced on a silicon surface subject to 40 keV Ar^+ irradiation at 15° (left column) and 60° (right column) for two ion fluence values and 3 mm away from the stainless steel plate. The length of the horizontal bars is 2 μm. The insets are the corresponding FFT images. The Fe flux comes from left to right while the ion flux goes from right to left as indicated by the arrows. Reprinted (figures 3(a) and (c)) with permission from [108], Copyright (2020) by the American Physical Society.

[121]. In agreement with results discussed above, very close to the mask edge, where the metal content is smaller, a nanohole-like pattern is induced. As we move towards the centre, a ripple morphology is found. This is explained by the fact that, at this midway location, the metal supply is still anisotropic, coming mostly from the closer mask edge. However, right at the centre, a clear dot pattern is observed since, here, the metal flux is isotropic. It should be noted that the specific mask design may affect the dot pattern [79, 122, 123].

This mask set-up allows one to perform systematic studies on the influence of certain variables on the pattern properties. One of them is the ion fluence. In these studies, the surface roughening and the pattern coarsening were characterized using either AFM or/and real-time GISAXS measurements [63, 79, 122, 124, 125].

Two different contributions were identified for the surface roughness (figure 14(a)). The most important one was due to the dot structures that initially increased, to then saturate for large enough fluences. The other, smaller, contribution operated at long-wavelengths, much larger than the dot size. The long-wavelength roughness can be glimpsed in figure 2(b) as well as in the images displayed in figure 15, in which dot patterns are obtained. Note how some dots are in dark zones (i.e. valleys) whereas others lie in brighter areas (i.e. protrusions). Thus, a long-wavelength roughness, spanning several inter-dot distances, develops under prolonged irradiation. The pattern wavelength can be obtained either from the GISAXS plots or from the PSD curves of the AFM images. In both of them, it can be identified as a peak whose position in the x-axis (the wave vector) may change with increasing fluence. This is shown in figure 14(b) where this wavelength is observed to coarsen with increasing irradiation, this coarsening being finally interrupted. The interrupted coarsening was found to be independent of the ion flux or the nature, amorphous or crystalline, of the silicon substrate. This property has attracted interest in the general field of pattern formation in nonlinear science [125].

As explained in the beginning of this section, the kinetic roughening and pattern coarsening were evaluated by obtaining the corresponding critical exponents. In these systems, α values in the 0.8–1.2 range, $\beta \sim 0.3$, and $1/z$ in the 0.2–0.5 range, were reported for the long wavelengths [63, 122]. However, this set of values failed to be consistent with the predictions of previous theoretical models. It should be noted that a similar long wavelength kinetic roughening was also observed when medium-energy Xe^+ ions were employed with a similar set-up [126]. Interestingly, for 20 keV Xe^+ ions the characteristic wavelengths observed were considerably larger than those found when 1.2 keV Ar^+ ion beams were employed. Thus, these length scales also increase with

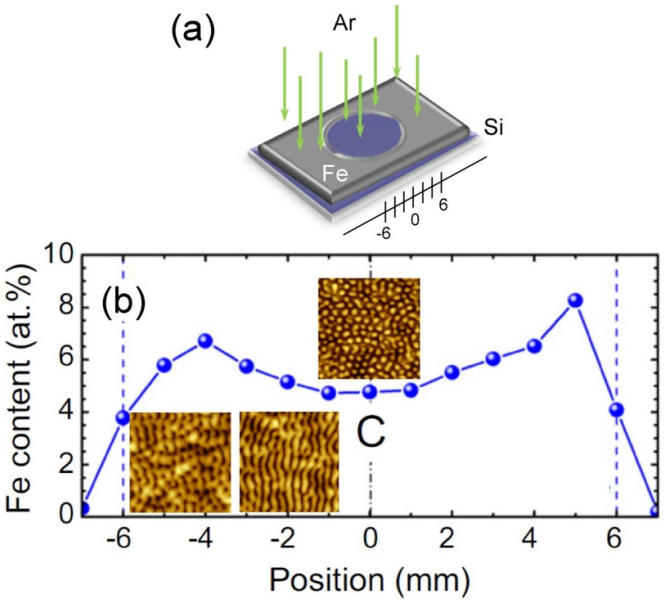

Figure 13. (a) Scheme of the sample-holder set-up showing the circular steel mask, the target surface as well as the incoming ion direction. (b) Axial XPS compositional profile from a Si(100) sample irradiated for 30 min ($\sim 2 \times 10^{18}$ ions cm^{-2}) at normal incidence under Fe co-deposition with a Fe mask with a hole diameter, $\phi = 12$ mm. The data have been extracted by scanning at different positions the relative intensity of the Fe2p and Si2p corelevels (normalized to the sensitivity factor). The insets from left to centre show 780 × 780 nm^2 AFM images taken close to the mask edge, midway between this location, and at the centre of the target surface (marked by C), respectively. Reproduced from [121].

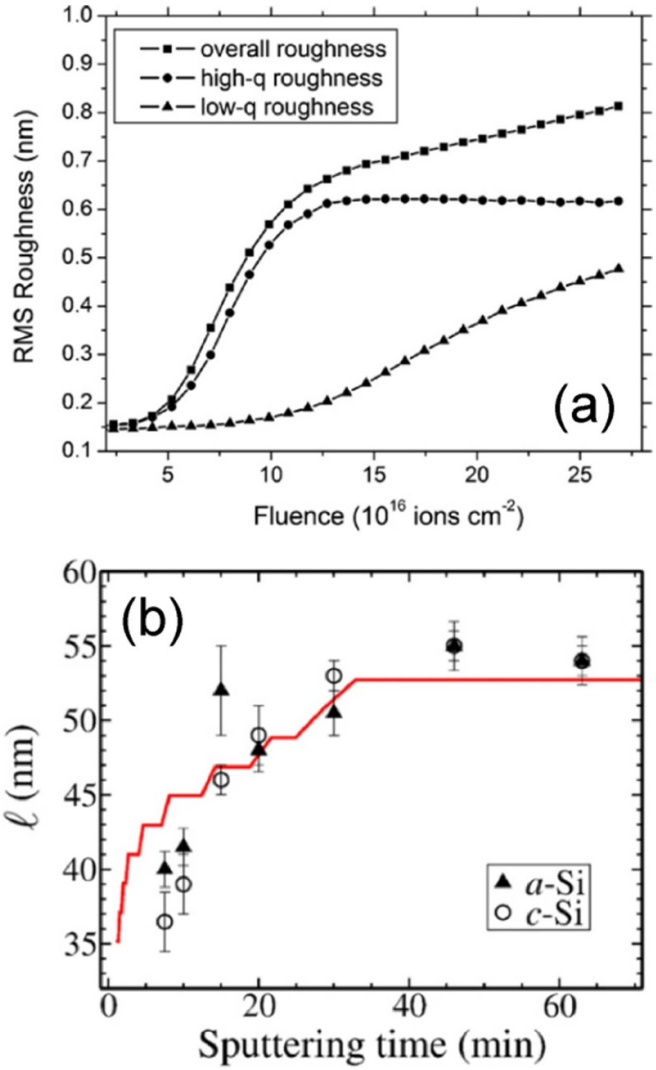

Figure 14. (a) Plot of the evolution of the roughness with ion fluence obtained from GISAXS measurements: the high-q contribution to the roughness is due to the dot structures, while the low-q contribution corresponds to long-wavelength fluctuations of the surface height, the overall roughness being the sum of both contributions. Reprinted from [122], Copyright (2007), with the permission from Elsevier. (b) Plot of the pattern wavelength versus ion irradiation time from AFM data for amorphous and crystalline Si surfaces. The red line represents the theoretical prediction of the model proposed in [125]. Reproduced from [125].

ion energy. It is worth noting that, due to the use of medium energy, it was possible to establish a correlation between this long wavelength corrugation and the local surface metal content [126]. In addition, the use of medium-energy ions in IBI with co-deposition set-ups produces taller nanostructures with higher aspect ratios, a fact that could be used for different applications [33, 127].

Another parameter that can be varied with this mask set-up is the diameter, ϕ, of the circular mask. In this way the metal flux at the centre of the Si target can be changed. This has an evident influence on the pattern as shown by figure 15. By varying the mask diameter, both the pattern wavelength and the long wavelength roughening change. In addition, as displayed in the same figure, the metal influences the pattern properties. For instance, by comparing figures 15(b) and (c), it is clear that a Mo mask leads to neater and more ordered patterns than a Fe mask. Likewise, the ion species has a strong influence on the pattern morphology as figures 15(c) and (d) evidence: indeed, when 1 keV Xe^+ ions impact on the Si surface with Mo mask, the dot size, the pattern wavelength, and the long corrugation change with respect to those obtained when bombarding with 1 keV Ar^+ ions. This has been confirmed for medium-energy Ar and Xe ion beams [126].

Finally, another parameter that has been studied is the target temperature during irradiation. Ozydin-Ince and Ludwig studied the pattern formation on Si surfaces bombarded at normal incidence by 500 eV Ar^+ ions with simultaneous Mo supply by GISAXS and AFM, from 25 °C up to 650 °C [84].

In figure 16 the real time GISAXS spectra obtained during the patterning process are shown. The spectra taken up to 350 °C display well-defined peaks associated with the growth of correlated structures, which are nanodots as the corresponding AFM images show. In addition, the large-scale corrugation is detected from the shoulders observed on both sides of the specular peaks of the GISAXS scans. From the analysis of the spectra, the height of the nanodots is seen to decrease with temperature from 1.7 nm down to 0.8 nm in the 25 °C–450 °C range. Accordingly, the surface roughness also decreases with temperature. The pattern vanishes for target

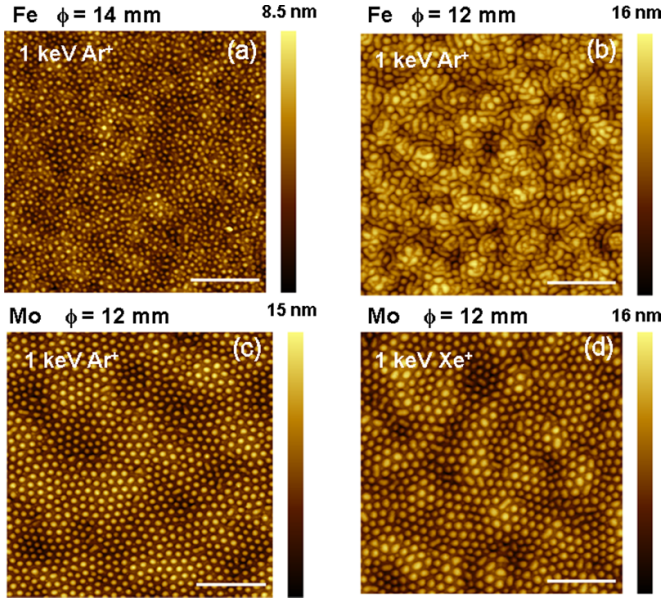

Figure 15. $2 \times 2\ \mu m^2$ AFM images of a Si target irradiated at normal incidence with a fluence of 6×10^{18} ions cm^{-2}: (a) with a Fe mask with $\phi = 14$ mm and 1 keV Ar^+ ion beam; (b) with a Fe mask of $\phi = 12$ mm and 1 keV Ar^+ ion beam; (c) with a Mo mask of $\phi = 12$ mm and 1 keV Ar^+ ion beam; (d) with a Mo mask of $\phi = 12$ mm and 1 keV Xe^+ ion beam and ion fluence of 4.5×10^{18} ions cm^{-2}. The horizontal bar represents 2 μm. Reproduced from [121].

temperatures equal to, or above 450 °C. A similar behaviour was reported earlier when the metal supply effects had not been recognized yet [128]. This behaviour is opposite to that reported for temperature effects on cone formation in metals, where ion bombardment mediated surface diffusion plays an important role [129–131]. In contrast, these results suggest that thermal energy promotes surface relaxation mechanisms.

3.2. Non-noble gas ion irradiation without metal co-deposition

The examples described above correspond to systems where the ion species was a noble gas. This type of ion is inert and, therefore, does not react with either the target or co-deposited atoms. However, in some cases, non-noble gas ions have been employed. Thus, in a sense, the target compositional heterogeneity is induced by the ion beam itself. Here, we can distinguish between ions that do react with the target atoms and those that do not.

3.2.1. Non-reactive ions. Depending on the target-ion species combination, different ions can be employed that, while not being noble gases, do not react with the target atoms. However, these ions behave differently since they are implanted and incorporated close to the target surface. This fact can affect the patterning process as these implanted atoms can have a different SY than the target atoms.

Perhaps, the most widely employed ion is Ga^+, because of its use in experiments with a focused ion beam (FIB), which usually allows one to follow the patterning process by SEM imaging and even to monitor the ripple propagation [132]. Thus, a Ga^+ ion beam has been employed to produce ripple patterns on Si [132, 133] and diamond [134] surfaces. It is worth noting that in these systems a ripple pattern was already produced for incidence angles below the threshold angle for pattern formation when noble gas ions are employed.

In contrast, when a Ge surface was irradiated with a 5 keV Ga^+ FIB system under normal incidence, a nanohole pattern was produced [135]. Moreover, in a later work the same group was able to produce similar patterns through the irradiation with a Bi^+ ion beam, with energies between 2 and 6 keV, but also by Ge^+ self-irradiation with ion energies in the 2–12 keV range [136]. As the authors stated, this fact proves that the driving force for nanohole patterning does not come from the implanted impurities. It is worth noting that amorphous Ge displays an enhanced swelling under IBI when compared to amorphous silicon [137], which can affect the IBI patterning [138].

A special case is the bombardment of a GaAs (100) surface with a 20 keV Ga^+ FIB at an incidence angle of 52° [139], since this surface is a compound and is being irradiated with ions of one of its elements. In this experiment, not only straight trenches are formed with increasing ion fluence, but they also become decorated at the top with self-assembled Ga-rich droplets, around 35 nm in height and 125 nm in width.

Other examples of this type of patterning are those of Si and Ge surfaces irradiated with an Au^+ ion beam [140–142]. In the work by Mollick *et al*, Au^+ ions were used on the Si or Ge surfaces with an incidence angle $\theta = 60°$. For Si targets, a mixed pattern of ripples with two orientations was produced. In contrast, for Ge targets the Au bombardment induced straight ripple patterns that were decorated at the top by gold agglomerates. The case of the Ge–Au^+ system is particularly interesting because of the excellent ripple pattern ordering that results from the coupling between the surface morphology and composition. Examples of these patterns are displayed in the top row of figure 17 where their FFT and ACF images are also included as insets to show the pattern ordering.

Another system where a non-noble gas ion was employed is that where a metal-cluster-complex, $Ir_4(CO)_7^+$, ion beam impinged at $\theta = 45°$ onto a Si surface with ion energies in the 2.5–10 keV range [143]. In this case, ripples form at low ion energies. The authors explain the pattern formation from the decrease of SY with decreasing energies, which leads to a higher implantation rate and the formation of a carbon-rich layer. As the SY is lower on the upwind ripple side than in the downwind one, this compositional patterning enhances the morphological one.

3.2.2. Reactive ions. There is another set of experiments with the same configuration but where the ion species reacts with the target atoms upon impinging on the target surface, leading to compound formation. In this way, both morphological and chemical surface patterns can be produced. The very first report, where O^+ ions were shown to produce ripple patterns, dates back from 1991, where such a pattern was induced

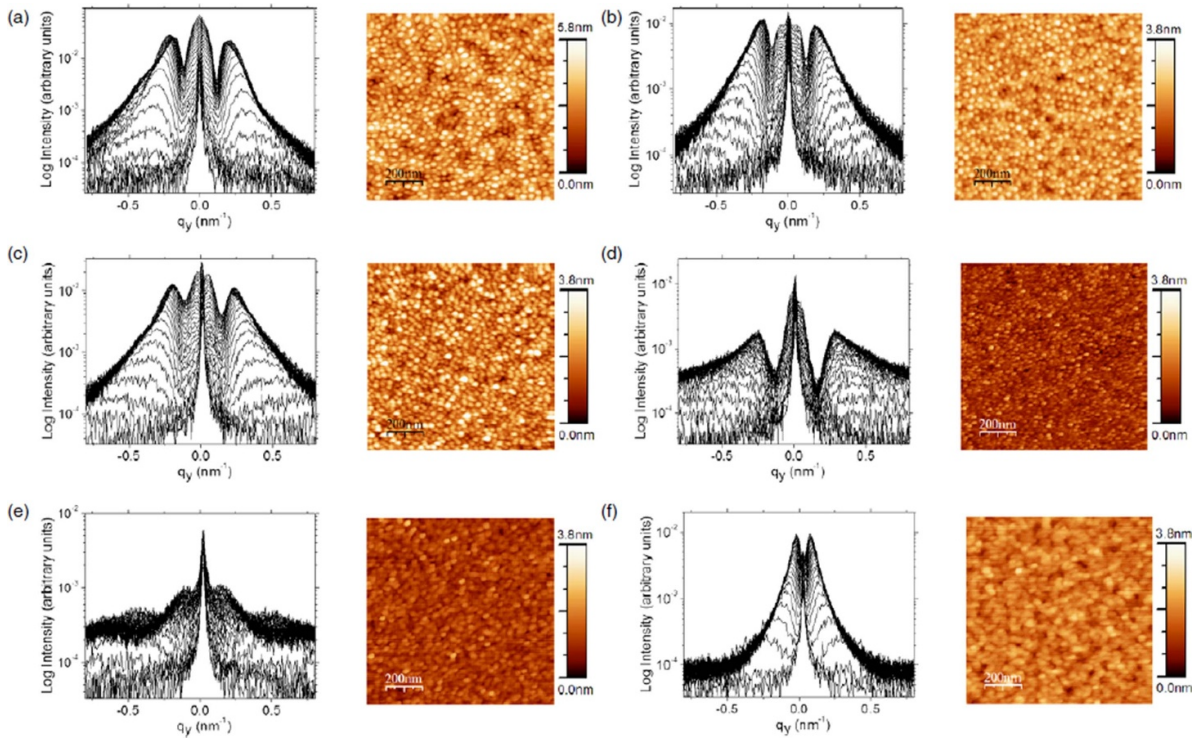

Figure 16. Real-time GISAXS and *ex-situ* AFM images of Si samples irradiated at normal incidence by 500 eV Ar^+ ions with simultaneous Mo supply at: (a) 25 °C, (b) 250 °C, (c) 350 °C, (d) 450 °C, (e) 550 °C, and (f) 650 °C. Reproduced from [84].

on a GaAs surface [60]. In this case, only the morphological pattern was reported. Some years later, an O^+ ion beam was also used to pattern ripples on a silicon surface [144]. Further studies on similar systems assessed the production of a chemical pattern, as Si-rich and silicon oxide-rich regions were evidenced by Auger Electron Spectroscopy [145] or current sensing AFM [146]. Another interesting report by Smirnov *et al* used nitrogen ions on silicon targets [147].

However, within the scope of this review, the most interesting system is that one where Fe^+ ion beams were employed on silicon targets. In this way, the ion beam and the metal supply have the same direction. In principle, the eventual silicide formation may cause further morphological instabilities and alter the pattern with respect to those obtained with noble gas ions. This is indeed the case, as shown by the study of the Si surface morphology bombarded by 40 keV Fe^+ ions at different incidence angles [109]. For instance, the threshold angle for ripple formation was smaller than those reported for Ar^+ and Xe^+ ions.

Furthermore, for incidence angles larger than the threshold value, the induced patterns displayed short-range hexagonal order, instead of the expected ripple shape [149]. Also, due to the Fe implantation the silicide-rich regions were rather localized on the surface, and close to the edge of the induced nanostructures [148–150]. This can be appreciated in figure 18 where localized Fe-rich regions (green in figure 18(a) and dark grey in figure 18(b)) are observed at the edges of the protruding nanostructures. The similarity between the images in figures 18(a) and (b) is remarkable, despite the fact that the silicon surface was ripple pre-patterned with an oxygen ion beam in panel (a).

The TEM micrograph of figure 18(b) shows zones with different dark-grey contrast. This feature is characteristic of silicon irradiation with medium-energy Ar^+ ions. Chini *et al* [151] reported similar observations for IBI of Si with 50–120 keV Ar^+ ions without concurrent metal co-deposition. These authors reported the presence of Ar bubbles inside the amorphized region, with larger sizes close to the surface, which accounts for the observed grey contrast modulation. The dark line at the bottom of the amorphized region corresponds to the rough a/c interface whose roughness increases with ion energy [151]. This dark line is also observed in figure 9. Both images in figure 18 also show a characteristic feature of surfaces irradiated with ion beams, namely the development of a saw-tooth surface profile along the projected ion beam direction. This morphology is also produced without foreign atom co-deposition, on different targets such as Si [152–156], Ge [12, 157–159], fused silica [160], mica [83, 161], carbon [162, 163] and aluminium [164]. This morphology appears under prolonged irradiation conditions, being enhanced at large ion beam incidence angles. This type of pattern morphology has been studied theoretically [165–167].

3.3. *IBI patterning of compound surfaces*

At this point, it is interesting to briefly present some of the results reported on IBI patterning of compound materials, such as GaSb, GaAs, or InP. In these cases, the target surface does

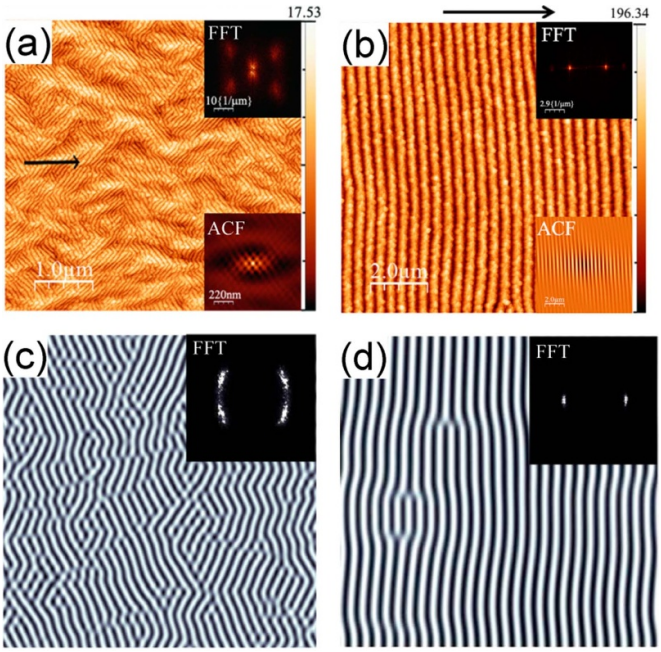

Figure 17. (a) AFM image of the pattern induced on Si surfaces after bombarding at 60° with a 26 keV Au^+ ion beam to a fluence of 2×10^{18} ions cm^{-2}; (b) AFM image of the pattern induced on Ge surfaces after bombarding at 60° with 26 keV Au^+ ion beam to a fluence of 4×10^{18} ions cm^{-2}. The corresponding FFT (top) and ACF (bottom) images are shown in the insets. The black arrows indicate the beam direction. The vertical scales are in nm. (c), (d) Gray-scale plots of the height h, resulting from a two-field model for different parameter values and integration times, resembling the corresponding experimental patterns in (a), (b), respectively. Reprinted from [140], with the permission of AIP Publishing.

not become compositionally heterogeneous due to the external supply of foreign atoms (either via co-deposition or via ion implantation) since itself is heterogeneous. Therefore, during the irradiation of these surfaces preferential sputtering effects can arise that eventually lead to the surface enrichment in one of the components and thus influence the pattern formation and development.

IBI ripple patterning of III–V semiconductors, such as GaAs, GaSb, InAs, and InP, had already been reported by the end of the last century [168]. However, the formation of hexagonally-ordered dots on GaSb triggered the renewed interest on these surfaces [9]. Thus, several studies appeared on the study of these patterns [80, 169, 170]. In particular, the induced dot patterns formed on the topmost GaSb layer were successfully transferred to an underlying Co layer resulting into an array of magnetic nanoparticles displaying short-range hexagonal ordering [171]. Also, studies on other semiconductor compound surfaces such as GaAs, InP, and InSb were done using low-energy or medium-energy ion beams [16, 172, 173].

Likewise, ripple patterns have been induced on SiC [174] and SiCo [175, 176] surfaces. In the latter case, the rippled surfaces displayed anisotropic electrical conductivity.

Special interest has been put into disclosing the mechanisms leading to dot formation of GaSb surfaces. In principle and according to the curvature-induced instability mentioned in the Introduction (and see section 5 below), in a compound surface the element displaying the higher SY should be more efficiently eroded from the surface troughs. Therefore, the dots should be rich in this element. In the case of GaSb, the dots should be Sb-rich. However, early studies reported dots to be Ga-rich due to the higher Ga mobility that leads to its segregation, resulting in Ga-rich dots due to its lower SY [177, 178]. However, El-Atwani *et al*, in a subsequent study, found that native oxide formation when these patterned surfaces were analysed *ex-situ*, i.e. exposed to air, led to preferential Ga oxidation and segregation. Therefore, these authors advised to perform characterization studies *in-situ* to avoid oxidation issues [179]. When low-energy ion scattering spectroscopy (LEISS) and XPS *in-situ* studies were performed, the data showed that in fact the surface became Sb-enriched once the oxidation effects vanished [180]. A later report on IBI patterning of III–V semiconductors (GaSb, GaAs, GaP) also with *in-situ* techniques, such as real-time GISAXS, XPS, LEISS [15], concluded that the surface instabilities were driven, rather, by a chemical instability inducing phase separation. In addition, by means of atomistic simulations, the authors suggested that ion-enhanced mobility associated with energy deposition by collision cascades could be the microscopic mechanism of this process [15]. Recently, this mobility issue on IBI GaSb patterning was addressed through experimental (GISAXS and angle-resolved Auger electron spectroscopy) and molecular dynamics simulations [181]. In this work, the simulations showed that, on the irradiated surface, Sb may be more mobile than Ga. The experimental results proved that the formation of an altered compositional depth profile becomes critical to produce surface morphological changes. Moreover, the simulations also showed that the compositional depth profile finally results into a phase separation process that drives the pattern formation.

Finally, another interesting feature of IBI patterning of semiconductor compound surfaces is the production of highly ordered patterns when the targets are irradiated at temperatures above their recrystallization temperature. Under these conditions, vacancies are created that then self-assemble driven by Erlich–Schwoebel barriers to surface diffusion [98]. Although this process is not exclusive of compound semiconductors, as it can also operate on Si and Ge surfaces, for instance, it does produce highly ordered patterns on GaAs(001) and InAs(001) surfaces [182, 183].

4. Experimental studies on the mechanisms of IBI patterning with metal co-deposition

Once the main systematic studies on IBI with compositional effects have been described, it is worth focusing on the case of IBI patterning with metal co-deposition. In particular, in this section we address the study of the relevance of the main experimental IBI parameters, such as target temperature and ion species and energy, on the pattern properties. Likewise, we will discuss the main mechanisms, and related experiments,

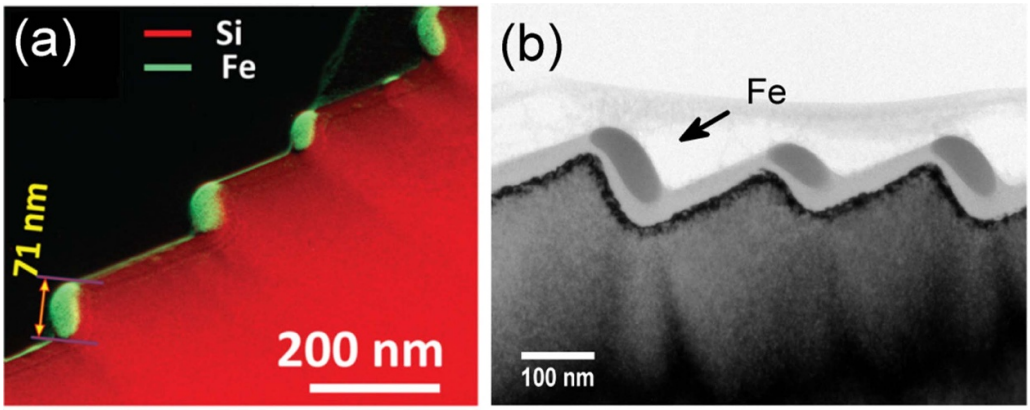

Figure 18. (a) Composite TEM + EDX image showing Si (red) and Fe (green) of a patterned Si surface produced by 8 keV O^+ ions with fluence 2×10^{18} ions cm^{-2} impinging at 60° and subsequent 36 keV Fe^{3+} implantation with fluence 10^{18} ions cm^{-2} at the same incidence angle. Reprinted from [148], with the permission of AIP Publishing. (b) Bright-field TEM image of a Si surface bombarded by 40 keV Fe^+ ions at 60° with fluence of 4×10^{18} ions cm^{-2}. Reproduced from [149]. CC BY 4.0.

invoked to play an important role in this pattern formation and development.

4.1. Target temperature

Since the seminal work of Wehner and Hajicek [184], it was already known that metal (e.g. Cu) surfaces subject to IBI with simultaneous addition of Mo atoms develop surface patterns consisting in an array of cones whose lateral dimensions span from the sub-micron up to the micron level. This type of pattern was also obtained on silicon surfaces using Mo as the additive atom [185, 186], as well as on other materials [187]. In general, this sort of patterning implies the use of relatively high target temperatures that can be induced by the high ion flux employed [188]. Thus, thermal energy activates surface diffusion of the added species, which results into cluster formation. These clusters have a lower sputtering rate (SR) than the target atoms, which then leads to pattern formation.

In contrast, in the systems addressed in this work, the target temperature is much lower (the ion flux being smaller) and instead of cones, with sizes in the several hundreds of nm or even microns, dot-like structures are produced with dimensions in the nm range. Furthermore, as shown in section 3.1.2 and [84, 128], the role of the target temperature in the latter case is clearly different from that played for cone formation. The studies addressing the role of target temperature in IBI production of dot patterns on silicon [84, 113, 128] yield a similar qualitative behaviour. There is an initial temperature range, from room temperature up to a value in the 150 °C–350 °C range, depending on the experimental set-up, where the dot pattern does not change appreciably. Then, for increasing temperatures both the pattern wavelength and dot height diminish until the pattern vanishes at higher temperatures in the 270 °C–450 °C range. In order to compare this behaviour with that obtained for IBI of silicon without concurrent metal co-deposition, we have to consider the case of ripple patterns since dot patterns are not produced under these conditions. The first studies were performed in ultra-high vacuum conditions and at target temperatures, in the 500 °C–750 °C range. These values are so high that recrystallization of the ion-damaged silicon occurs much faster than amorphization during IBI [189]. On Si(100) surfaces, it was obtained that the wavelength increased with temperature due to a surface diffusion mechanism [99] whereas on Si(111) surfaces a more complex behaviour was observed as the pattern morphology evolved with temperature and changed its orientation [100]. The other report to be considered deals with a temperature range from room temperature up to 350 °C [190], which is similar to those employed for IBI with concurrent co-deposition. In this work, it was found that the surface roughness was constant up to 350 °C to decrease for higher temperatures. In contrast, the wavelength increased initially up to a temperature of 100 °C but remained constant in the 100 °C–350 °C range. This behaviour, which does not obey the expected Arrhenius dependence found for higher temperatures [99], is quite similar to that found for the dot patterns.

4.2. Ion energy and nature

From the data presented in section 3, the influence of the ion energy and nature on the induced patterning can be discussed. Regarding the ion nature, from the comparison of the different reports, as long as noble gas ions (Xe^+, Ar^+, or Kr^+) are employed there are not essential differences in the produced patterns and trends. However, in the only study using two different ions with the same set-up [126], differences did arise on the patterns produced with metal co-deposition, particularly in terms of ordering.

The scenario changes when the IBI is performed with non noble gas ions. In this case, the ion can react with the target atoms, as in the case of silicide formation described in section 3, which can lead to preferential sputtering processes and, therefore, to surface instabilities development. Moreover, even in the case that the incoming ions do not react with the target ones, they become implanted. Therefore, the target surface becomes compositionally heterogeneous, with two types of atoms with different SRs, which also may lead to instability development.

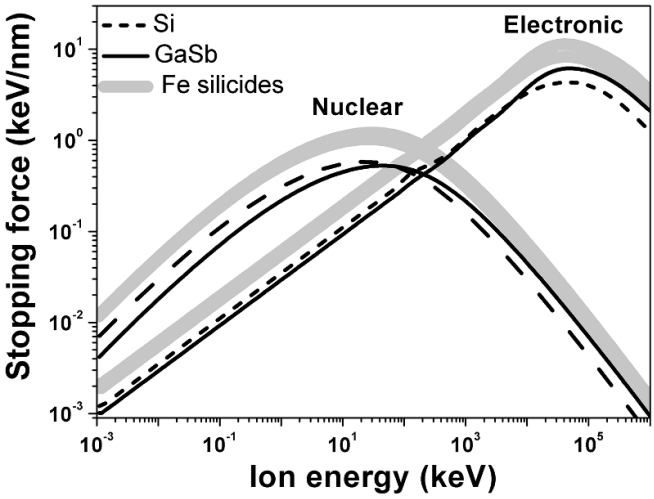

Figure 19. Nuclear and electronic stopping force calculated by SRIM code for Ar ions impinging into Si (dashed line), GaSb (solid line), and different iron silicides (light grey). The dependence of GaSb is similar to those of GaAs and InP. Iron silicides are represented by the light grey band that corresponds to three compounds with different stoichiometry ($FeSi_2$, FeSi, Fe_3Si) following the data by Moroni *et al* [193].

The ion energy range sampled in the experiments showed in section 3 varies from the low-energy range (close to the 1 keV) to the medium-energy one (up to 40 keV). It should be noted that the use of low energy ion guns does not allow to study any dependence over a wide ion energy range whereas it is more accessible when working with medium-energy IBI facilities. In general, the employ of medium-energy does not affect the trends observed when low-energy ions were used. Thus, the patterns evolve similarly with increasing distance to the metal plate (i.e. ripple-dot-flat sequence). Likewise, the ripple orientation in all cases is defined by the foreign atom flux. In addition, the induced protruding nanostructures are silicide-rich.

However, when the medium-energy was varied from 20 keV up to 160 keV Xe^+ IBI [126], the induced pattern was quite disordered for 80 keV Xe^+ IBI and vanished when 160 keV Xe^+ ions were employed. This fact could be related with the relative weight of the nuclear and electronic stopping forces. In figure 19 are plotted these stopping forces simulated with SRIM software [191] for three crystalline target systems, namely Si, GaSb and iron silicides, for Ar^+ ion energies varying over 9 orders of magnitude. It should be noted that these data are obtained for the corresponding crystalline surfaces, whereas during IBI the surfaces become amorphized and, therefore, their density can be smaller. For ion energies up to 40 keV the nuclear stopping force is at least five times larger than the electronic one, which corresponds to most of the ion energy values of the reports included in this work. However, for larger ion energies this difference decreases to disappear at roughly 200 keV. For even higher energies the electronic stopping dominates. Therefore, depending on the ion energy, different processes can take place, whether nuclear mechanisms (collisions cascades leading to sputtering) or electronic ones (e.g. thermal spikes producing defects) are dominant [192]. Interestingly, for the systems related to metal co-deposition, similar trends for the relative weight of both stopping forces are found for Si and iron silicides.

However, what is evident from the reported data, particularly when nanodot patterns are produced, is that higher ion energies lead to the production of larger nanometre-sized nanostructures (in terms, for instance, of dot diameter and height) and the characteristic distance of the longwave corrugation. This fact implies a clear advantage for analysing the patterns with compositional and morphological techniques. Due to the larger nanostructures dimensions, it becomes easier to correlate the morphological and compositional data [108, 126].

4.3. Stress

One of the first studies of the role played by the stress is due to Ozaydin *et al* [105]. In their report, they performed stress measurements on samples bombarded with simultaneous Mo seeding that showed initially a compressive stress, to finally change to a larger tensile stress upon further irradiation. They associated this behaviour to the formation of higher density regions around the Mo seeds and considered it as playing a dominant role in nanodot patterning.

4.4. Chemical effects

At that time, Ozaydin *et al* did not check the eventual formation of a silicide between Si and Mo, but just commented that this could be possible. This, in fact, proved to be a key issue towards the understanding of this patterning process. Silicide formation during the ion irradiation of silicon with simultaneous metal co-deposition was first assessed by Sánchez-García *et al* [194]. Afterwards, this fact was confirmed in different reports on the subject. However, its role in the patterning process has remained a controversial issue. More specifically, the question was whether silicide formation was necessary for the surface patterning or not.

In exhaustive experimental works, the patterning of silicon surfaces with different metals as foreign co-deposited atoms was studied [13, 114]. These authors employed the set-up of the adjacent metal plate described in section 3. They chose carefully the metals to be co-deposited since they employed both silicide forming metals (Fe, Mo, Ni, W, and Pt in [114], and Pd and Ir in [13]) and non-silicide forming ones (Cu and Au, and Ag and Pb, respectively). In both studies, the metals were chosen in such a way that there were similar metals in the two groups regarding their collision cascade behaviour, enabling the discrimination between collisional and chemical effects. The authors concluded that only the silicide forming metals led to surface patterning. This finding was in line with previous results where surface patterning was achieved using either Mo or Fe [13, 63, 79, 80, 84, 85, 87, 105, 108, 109, 113–117, 120–123, 126, 149, 150, 194]. However, no pattern was formed on Si surfaces by using C, which forms a stable compound with Si, nor with Au or Cu as foreign atoms on Si. Consequently, the authors concluded that silicide formation was a necessary condition for surface patterning. Likewise,

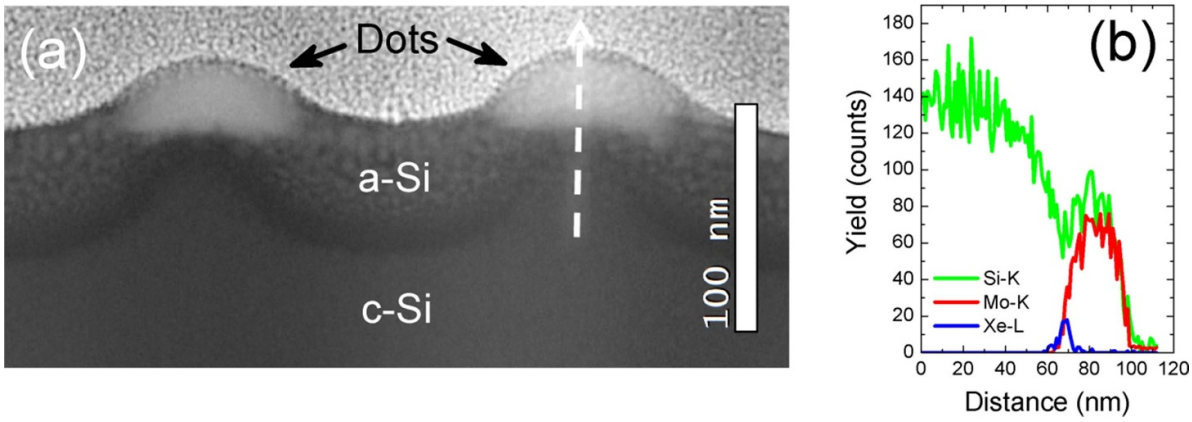

Figure 20. (a) TEM image of a Si surface after being irradiated with a 40 keV Xe^+ ion beam with Mo co-deposition, in which two close-by nanodots are observed. Note the three grey levels: the darkest one, at the bottom, corresponds to the bulk c-Si, the intermediate granular one indicates the a-Si layer amorphized by the incoming ions, whereas the brighter one corresponds to the silicide-rich regions on the dots. (b) EDX scan line profiles of Si (K), Mo (K) and Xe (L) through the white dashed arrow depicted in figure (a). Reproduced from [126].

they concluded that the atomic mass of the foreign atom was largely irrelevant.

However, this scenario is questioned by other reports where surface patterning occurs even when silicides do not form [195, 196]. A special case is that of gold, which does not form a silicide and was reported not to lead to surface patterning [114], although this fact is questioned [197]. Thus, El-Atwani *et al* performed a series of experiments where an ultrathin metal layer was deposited on a silicon surface and irradiated at normal incidence by 200 eV Ar^+ ions. They studied different metals as capping film, namely Au, Fe, Ni, and Cu [197–199]. They found that irradiation led to the mixing of the metal and Si atoms, silicide formation, and nanodot formation in all cases. In addition, these authors correlated the silicide binding energy with the threshold amount of impurities needed to trigger the nanodot formation. It is worth noting that Engler *et al* did not find that the enthalpy of silicide formation was relevant for the patterning capability, although they also reported that a rather low value could lead to the absence of patterning [13].

4.5. Preferential sputtering

One physical process strongly linked with the influence of silicide formation on IBI nanopatterning is its different SY with respect to that of the target Si surface. It has been assumed that the SY of the silicide is lower than that of the surrounding Si regions. Consequently, the silicide-rich regions emerge and protrude with respect to Si rich regions that are more effectively sputtered away. This scenario agrees with different experimental reports where the top of the ripples or dots are seen to be silicide-rich. In particular, this is confirmed experimentally for the case of nanodot production using medium-energy (40 keV) Xe^+ ions impinging normally on the Si surface with Mo co-deposition. These conditions lead to larger nanostructures that are better and more easily imaged by microscopy techniques like TEM [126]. Figure 20 shows a scanning TEM (STEM) image of two of these dots.

What is interesting in figure 20 is the compositional profile across the dot structure, compared to that across the region between dots. Across the dot, from the top we find the bright silicide-rich region, then a thin (or almost null in the left dot structure) a-Si layer, where Xe atoms are implanted, to reach the undamaged c-Si region. In contrast, between dots, the a-Si layer is much wider. This difference means that the silicide-rich dot structure shields the underlying layers from the ion beam, which is due to its low SY, which leads to the small Xe content just below the dot structure in figure 20(b).

Despite these evidences, attempts to actually measure and compare the SY of Si and silicide surfaces yield the opposite behaviour [200]. In this work, the authors deposited by sputtering silicide films with three different stoichiometries and measured their SR under irradiation with a 1 keV Ar^+ ion beam at normal incidence, and compared them with that of a silicon wafer. For that purpose, masks were used to measure the sputtered depth. The analyses showed that the SR of the three silicides was higher than that of the Si. This was confirmed by simulations using TRYDIN [201], in agreement with previous simulations [121]. On the other hand, Engler *et al* [13] carried out simulations with TRIMP.SP [202] stressing the fact that in the actual experiments the metal is continuously supplied onto the irradiated Si surface. Therefore, they argued that a dynamic equilibrium should be assumed (i.e. a constant silicide stoichiometry), which is not the case with TRIMP.SP. Moreover, they also stated that density of the material must be taken into account. Correspondingly, they introduce the magnitude $\rho_{Si} = Y_{Si}/n$, where Y_{Si} is the partial Si sputtering within the silicide and n the density of the material. With this approach, they did obtain that the silicide was eroded at a slower pace than the pure Si patches, in agreement with the experimental evidence [112–114].

One report that, somehow, collides with these findings is due to Moon *et al* [196] because these authors also employed Au as co-deposited metal, using the plate set-up. Furthermore, they employed such irradiation conditions, $\theta = 75°$, that the SY of gold and Si is the same. They obtained ripple patterns

that change orientation for locations which are close enough to the gold plate. One possible relevant detail is the large angle between the ion beam and the gold flux. Bradley showed that a generalization of the Sigmund model of ion sputtering that takes into account the effect of the deposited surface impurities on the collision cascades, combined with his previous theory of IBI with concurrent atom co-deposition [203], predicts a sequence of surface patterns as the impurity content changes similar to that found by Moon *et al* [204].

4.6. Early stages of pattern formation: phase segregation and height fluctuations

Despite the, in some occasions, controversial reports, it is accepted that the formation of silicides triggers the pattern formation. However, there are discrepancies about the early stages of the surface patterning. We have mentioned in section 4.3 the model proposed by Ozaydin *et al* that invokes the tensile stress produced around the Mo seeds, which can also occur in silicide patches on the irradiated surface, as a possible pattern trigger mechanism. Two more main processes have been proposed. First, Hofsäss *et al* highlighted ion-induced phase segregation, which would form silicide-rich patches on the irradiated surfaces, followed by the above explained preferential sputtering of Si with respect to that of silicides, to lead to pattern formation [114]. However, further experimental work using GISAXS, which is sensitive to surface topography as well as to the lateral variations of the electron density and, therefore, to any phase separation taking place during the irradiation, concluded that phase segregation occurs simultaneously, and not previously, to ripple formation [205]. Moreover, the experiments carried out by Engler *et al* using foreign metal atoms prone to silicide formation, such as Fe, evaporated on the Si surface at different angles with respect to the ion beam (figure 6), provides useful information on the possible mechanisms behind this patterning process [13]. The fact that the pattern formation depends on the relative angle between the two applied beams suggests that phase segregation is not the unique driving process. Macko *et al* [113] had already proposed that height fluctuations caused compositional ones. Thus, probably, pattern formation in the presence of impurities would be due to a synergetic effect between height and composition fluctuations. Composition fluctuations induce height fluctuations and vice versa, the coupling being bidirectional. Since height fluctuations are quite affected by the specific geometry of the experimental set-up, this scenario agrees with the large variety of patterns reported so far. Moreover, as discussed by Engler *et al*, the interpretation of the different parameters affecting the pattern formation, such as relative fluxes of metals and ions, metal nature, angles involved, distance to the metal source, and metal content, may be convoluted as many factors can come into play.

Finally, another effect, which indeed plays an important role when impurities are deposited during irradiation, is the change of the collision cascade due to the presence of implanted ions. This effect can be glimpsed in figure 20 by comparing the thickness of the a-Si layer below and between the dots. This effect was invoked to play a role [117, 199] and has been also considered in theoretical models [204, 206].

5. Theoretical modelling

As the previous sections show, multiple mechanisms can come into play to trigger IBI nanopattern formation with compositional effects. Therefore, the development of models that capture this complexity is a challenging task. We will describe the different approaches tried so far to account for this patterning process.

We will mainly focus on the so-called continuum models that describe the time evolution of the surface height, which is described by the function $h(x,y,t)$ where (x,y) are the spatial coordinates in the target plane and t is the irradiation time. These models describe the temporal change of the height, $\partial h/\partial t$, via an evolution differential equation in which different terms appear which are functions of the space derivatives of h ($\partial_x h$, $\partial_y h$, $\partial_x^2 h$, $\partial_y^2 h$, etc), and are associated with different physical processes, like the dependence of the SY on the local surface slope, surface diffusion, viscous flow, etc [6].

This approach has been largely used for the case of noble gas IBI patterning of mono-elemental surfaces (i.e. without compositional heterogeneity). A seminal model is due to BH [43], who, based on the dependence of the SY on the local surface curvature, proposed the equation:

$$\partial_t h = -\upsilon_0 - \nu_x \partial_x^2 h - \nu_y \partial_y^2 h - B\nabla^4 h \qquad (1)$$

where υ_0 is the average erosion rate, and B is related to thermally-activated surface diffusion. The other coefficients are related to the Gaussian distribution of the energy deposited by the ions [41]. The second derivative terms contain the dependence of the sputtering on the local surface curvature, where the local surface minima are sputtered faster than the maxima for positive ν_x and ν_y values, as already noted by Sigmund [42]. Equation (1) was able to predict different experimental behaviours. However, it cannot describe the full dynamics of the patterning process since it only contains linear terms in the height and its derivatives, so that the height field diverges exponentially under pattern-forming conditions [207]. After this proposal, different elaborations, based in the continuum framework pioneered by BH, have been proposed that include both linear and non-linear effects (see [6] for a review). One of the most relevant ones was that one proposed by CV to account for the surface mass transport induced by the incoming ions [46]. This effect causes no patterns to be produced below a threshold incidence angle, a limitation that is bypassed when metal co-deposition takes place.

One further refinement that had consequences on the modelling of IBI pattern with metal co-deposition is the proposal of two-field models. The previous models are single-field since they consider just the evolution of the height. However, following an observation already found in [2], Aste and Valbusa [208] pursued the resemblance of surface erosion by impinging ions with the formation of Aeolian and underwater sand ripple patterns [209]. This analogy lies in the existence

in both cases of immobile and mobile particles (atoms/sand grains). For the case of the sand dunes, this allows one to describe the pattern dynamics by coupling the evolution of the height with that of the density of species that are transported at the surface. As noted at the end of section 2, in IBI, it is well known that ion irradiation of semiconductor surfaces, such as Si or Ge, causes the formation of a thin amorphous layer [6]. This layer can undergo, for instance, ion-induced viscous flow [47], i.e. their atoms are mobile to a certain extent depending on the mechanisms in operation. These concepts have been used to develop two-field models for IBI patterning without simultaneous foreign atom deposition, with one field being the surface height and the second one being the density of mobile species within the amorphous layer. This has been applied for both normal [77, 210] and oblique [211, 212] ion incidence conditions. In many of these cases, and thanks to the quite different time scales of the erosive and diffusive processes, it is possible to derive a single evolution equation for the height, akin to equation (1), in which the coefficients of the different terms that appear can be related to experimental parameters. In fact, one of these equations proposed for normal incidence even reproduced quantitatively the dynamics obtained for such condition with metal co-deposition, despite not including any specific term related to the additional metal supply [124]. As noted before [6], such agreement is possible because these equations describe large-scale behaviour, for which universality usually occurs [207]. This implies that systems with different microscopic nature may display similar large-scale properties.

The most relevant aspect of two-field models for the advance in the description of IBI patterning with compositional heterogeneity is that they allow to describe both, the height and the composition of the surface. Regarding the latter, if there are only two species, A and B, such as silicon and silicide, the compositions of the two species are constrained by a conservation law. Therefore, with just two equations (for h and, say, the concentration of A) the dynamics of the full system can be described.

5.1. IBI of binary targets

Chronologically, the first attempt along this line was on modelling IBI of a binary compound, such as alloys [103]. In this model, only linear terms are considered in the height and composition fields and their derivatives. Shenoy *et al* obtained that, in addition to ripple development, and depending on the differences in SY and surface diffusivities of the alloy components A and B, a modulation of the surface composition will arise that can be in or out of phase with the ripple periodicity (figure 21).

In the wake of this pioneering work, Bradley and Shipman published a series of papers in which they developed and refined the two-field model to explain the patterns observed in compound materials, such as those obtained by Facsko *et al* [9] on GaSb under normal incidence irradiation [213–215]. They included non-linear terms that are necessary to saturate growth and produce e.g. hexagonal ordering. Thus, they proposed two coupled evolution equations with different terms

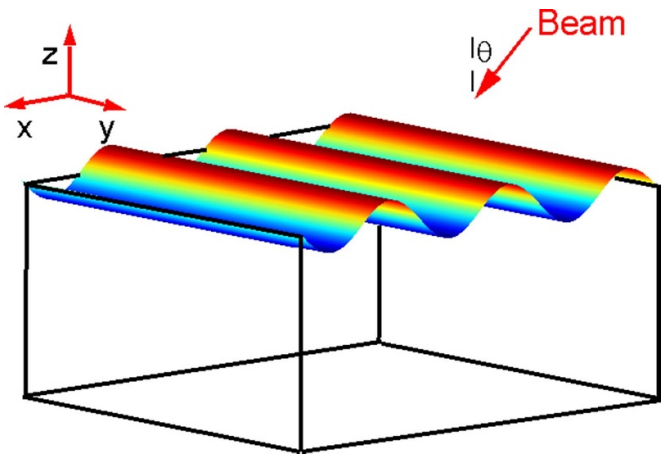

Figure 21. Three-dimensional representation of a ripple pattern formed on an alloy surface with a wave vector along the projected ion beam direction impinging at an angle of θ. The ripple pattern will also lead to gradients in composition marked by colour variations. Reprinted (figure) with permission from [103], Copyright (2007) by the American Physical Society.

whose coefficients depended on different parameters. Depending on the values of these parameters (see figure 22) they obtained nanodot patterns displaying short-range hexagonal order or even ripples, despite the normal incidence condition. These examples show how different pattern morphologies result depending on the relative weight of the coefficients of the terms in the continuum equations. The key to produce these patterns is the coupling between the surface topography and a thin surface layer of altered composition [103, 214]. In the case of nanodots, it was found that their top structures were rich in the species with the higher SY. Furthermore, they obtained that the nanodot pattern coarsens with time for certain ranges of parameters, as it occurs in many experimental cases.

In a later study, the same authors addressed the large degree of hexagonal ordering of the dot patterns by including a CV term accounting for the ion-induced diffusive currents. In this way, the range of unstable height modes becomes considerably narrowed [215]. This is known to improve largely the degree of in-plane ordering [207]. Examples of the ordered patterns that can be reproduced by the model are shown in figures 22(c) and (f).

In most of the previous models, the surface instability is due to the SY unstable curvature dependence as noted by Sigmund [42]. In a further development of the theory, Bradley addressed a situation in which this was not the case [216]. He found that, even under this assumption, a surface instability can take place if SY amplification occurs, namely, there is a mix of heavier atoms with a lesser contribution of lighter atoms. Then, the former will backscatter more ions than the latter, resulting in collision cascades that are more concentrated near the surface of the solid. In this way, the addition of heavier atoms can produce an SY increase of the lighter atoms. Under this assumption, a disordered array of nanodots forms, with the lighter of the two atomic species being concentrated at the peaks of the dots.

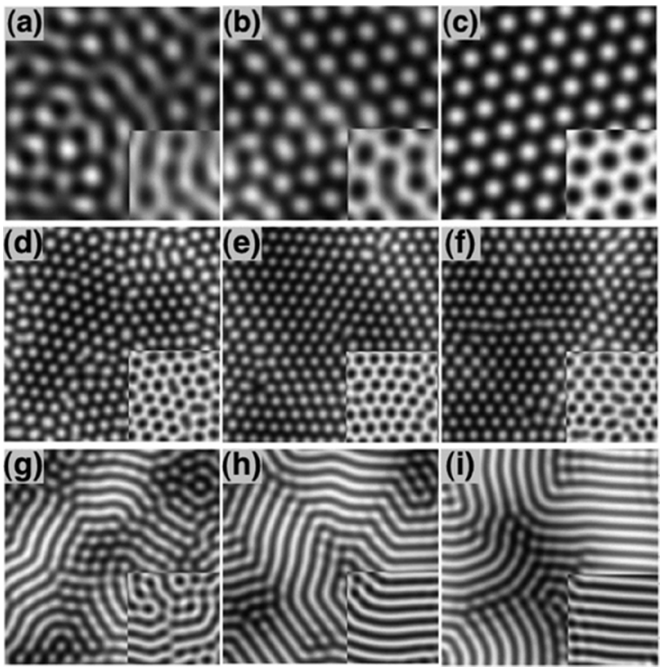

Figure 22. (a)–(i) Gray-scale plots of the target height for the model by Shipman and Bradley of an irradiated binary target for different parameter and time values. Insets: gray-scale plots of the compositional field superimposed over the topographical one. In all plots, the shading is light (dark) where (h) or the compositional field is large (small). Reprinted (figure) with permission from [214], Copyright (2011) by the American Physical Society.

Finally, a further generalization of the model by Bradley and Shipman was proposed by Norris [217]. In his proposal, the effect of ion-assisted phase separation was included. A chemically driven finite-wavelength instability was found that can explain the order of observed patterns, even when the erosive Bradley–Harper instability does not operate. In this case, those atoms with a lower SY remain at the top of the dots.

The above models were mainly motivated to explain the large degree of ordering of the GaSb nanodot patterns reported for normal incidence conditions in [9]. In a further development, the same approach was applied to study the generation of highly ordered ripple patterns when a binary compound was ion bombarded at oblique incidence [218]. In this case, the authors found that a high degree of pattern ordering could also be achieved, provided that variables such as ion species, energy and angle of incidence were appropriately chosen.

5.2. IBI with concurrent atom co-deposition

The first models addressing IBI patterning with metal co-deposition were discrete Monte Carlo ones [219, 220]. In these works, it was shown that a great variety of situations (i.e. patterns or surface morphologies) could, in principle, be generated depending on the processing conditions.

As mentioned above, continuum two-field models were initially intended either for IBI patterning of mono-elemental semiconductors or for binary compounds. However, their fundamental basis, i.e. the coupling of two fields, namely height and compositional fluctuations, makes them, in principle, very adequate also to address IBI patterning with simultaneous co-deposition, either when a compound is formed (as in the silicide cases) or when the two species (target and co-deposited) do not react. Within this framework, the first continuum model proposed was due to Zhou and Lu for normal ion beam incidence [221]. In their two-field model, Zhou and Lu incorporated curvature-dependent (BH) erosion, ion-induced smoothening (CV), and ion-enhanced viscous flow as the basic processes operating during standard ion sputtering, while Fickian diffusion of the mobile species through the surface layer was neglected. They also included two more effects related to the metal incorporation, namely, the surface stress-induced instability [105] and preferential sputtering. From their results, the authors concluded that BH and stress effects overcome the stabilizing ones, thus leading to pattern formation and development, aided by preferential sputtering effects.

In a further step, Bradley proposed a linear model for the early-time dynamics of IBI patterning of a flat surface under seeding conditions and normal ion incidence [222]. He assumed that the foreign atoms, once deposited on the target surface, become immobilized. This choice was adopted on the basis of the then suggested fact that Mo atoms formed silicides on silicon targets. In addition, surface diffusion was included as a stabilizing mechanism. Within this scenario, the foreign atoms, due to their immobility, will be sputtered away more efficiently at the surface depressions than at the protrusions due to the BH effect, which leads to the surface destabilization. In this work, it was obtained that a certain threshold flux of the foreign atoms is necessary to destabilize a flat surface, overcoming the stabilizing effects of the CV mechanism. This behaviour agreed with experimental observations, see section 3. This threshold flux value did not depend on the target temperature, but did depend on the SY of the foreign atoms.

In a next theoretical model, Bradley addressed the case of a target surface subject to normal, or near-normal-incidence ion bombardment with simultaneous oblique supply of impurities [203]. In this case, the BH and CV terms, as well as the thermally activated surface diffusion, were not included while surface viscous flow was considered. It was assumed that the impurity did not react with the target atoms, therefore excluding, in principle, those cases concerning silicon targets and Fe or Mo as seeding atoms. Once more, the model was based on a linear equation, thus concerning the early-stages of surface patterning. The aim of such a model was to address the experimental reports of ripple formation for a surface under ion beam bombardment at normal incidence with simultaneous impurity supply. The main result of this model is that a surface instability does take place, which is not caused by the BH effect but rather is a consequence of the different SY of the target and the impurity atoms. In fact, in the model those atoms with a lower SY will accumulate at the ripple crests. These predictions indeed are supported by experimental evidences obtained on silicon with metal impurities prone to form silicides. However, as stated, the model does not consider this situation. In addition, for the case of IBI of Si with simultaneous Fe supply, the SY of Fe is higher than that of Si. Therefore,

the agreement of the model with the experimental data is not clear.

This problem was overcome in a further model by the same author [104]. Now, the model considers the case of a target surface irradiated at normal—or close to normal—incidence with oblique supply of metallic impurities that do react with the target atoms to form a compound. The aim of this final model is clearly to address the case of Si irradiated surfaces with oblique supply of metals such as Fe and Mo. In fact, it is assumed in the model that the SY of the compound is smaller than that of the target atoms, as it occurs in the Si/Fe and Si/Mo cases. This time, the model does include the CV and radiation-induced viscous flow but it does not include the BH term nor thermally activated surface diffusion. The suppression of the BH term is intended to prove that ripple formation can take place even when the dependence of the SY on the surface curvature does not operate. What results of the linear instability analysis of this model is that a ripple instability may occur, provided that the impurity flux, j, is larger than a threshold value, j_c, in order to overcome the CV stabilizing effect. Furthermore, it predicts the ripples to be oriented with their wave vector parallel to the projected deposition direction. Ripple formation is due to the interplay between the surface topography and surface composition. Thus, the impurity flux will be greater at the higher sloped surface locations facing the incoming flux. As a compound with a smaller SY is formed, those locations will be eroded at a slower pace than those locations receiving a lower impurity flux (such as valleys and sloped surface regions not facing the impurity flux). In this way, the compound will accumulate at the ripple crests that will be eroded at a lower rate, which will lead to ripple development. Some of these predictions were reported experimentally [112, 113]. In particular, the interplay between morphology and surface composition was also proposed, from experimental studies, by Engler *et al* [13]. Finally, the model also proposed that the ripple wavelength depended on impurity flux as $\lambda \propto [j - j_c]^{-1/2}$ for j values close to the threshold impurity flux for pattern formation. This dependence was later confirmed experimentally [108].

Although a significant advance has been reached in the modelling of this IBI patterning, there is room for further developments. The results of the analysis are mostly based on a linear approximation, which implies that only the early stages of the patterning process are considered. Thus, a theory that would address later stages of patterning is still missing. Likewise, in some of the models some contributions are neglected while others are included and vice versa in still different models. It would be interesting to develop a model that systematically includes the main mechanisms operating under standard conditions in IBI experiments. Another very important issue, as will be shown below, is that related to the high degree of spatial ordering that can be achieved in this nanopatterning technique. To this date, there are no models aimed at understanding such enhanced order properties.

A related example is the two-field modelling of the patterns produced on Si and Ge surfaces irradiated by an Au^+ ion beam at an incidence angle of 60°, which have been described above [140]. As mentioned above, on silicon targets a mixed pattern with ripples at two basic orientations was produced, whereas on Ge surfaces a straight, parallel ripple pattern was induced (see figure 17). In this case, a two-field model was able to simulate surfaces with striking resemblance to that of the experimental patterns as illustrated in figure 17. This example shows the potential behind the use of two-field models in this type of IBI patterning. As noted in section 3.2, the amorphized Si and Ge surfaces display a quite different swelling behaviour upon IBI. Therefore, these examples are not shown for comparison purposes.

6. Special features

In this section, we will comment two additional important issues that seem, at the present moment, exclusive of IBI patterning with concurrent co-deposition, namely the enhanced pattern order and the development of a chemical pattern simultaneously with the morphological one.

6.1. Pattern ordering

Figure 17 exemplifies one of the most appealing features of IBI with metal co-deposition, which is the high degree of ordering that can be obtained, depending on the experimental conditions, such as the target and ion species, irradiation angle, experimental geometry, etc. Usually, the ripple patterns produced by IBI patterning without impurity co-deposition display an important number of defects and do not feature a large degree of order. The disorder appearing for large fluences [11, 223] is associated with the nonlinear nature of the pattern formation process [224, 225]. Thus, only a relatively narrow window of fluences is useful to improve the pattern ordering. Accordingly, specific experimental configurations have been devised to improve this ordering, like the sequential ion-beam sputtering method [226], or target rocking [227, 228]. Following this strategy, unconventional formats for IBI patterning have been developed in order to increase the pattern ordering [229]. Recently, the pattern ordering has been improved by IBI of a bilayer target system, compared to that obtained on either of its single layers [230]. Also, it is worth mentioning that theoretical studies on IBI of binary compounds predict that a great order enhancement could be achieved with an appropriate choice of ion species, energy, and angle of incidence [218]. It is important to stress that the reports mentioned above refer to ripple morphologies, while from [9] it is clear that nanodot patterns of great regularity and order can be produced by IBI on binary compounds.

The case that mainly concerns this review is somewhat different. It is well known in the scientific community working in the field that highly ordered patterns can be achieved with IBI with metal co-deposition. Furthermore, not only ordered ripple patterns can be produced but also nanodot ones.

In particular, the works by Ziberi *et al* do show patterns, both of ripples and dots, with an astonishing degree of ordering on both Si and Ge surfaces [67, 231–233]. Examples are displayed in figure 23 where the high ordering of ripple and dot patterns is evident. These patterns were obtained with a broad

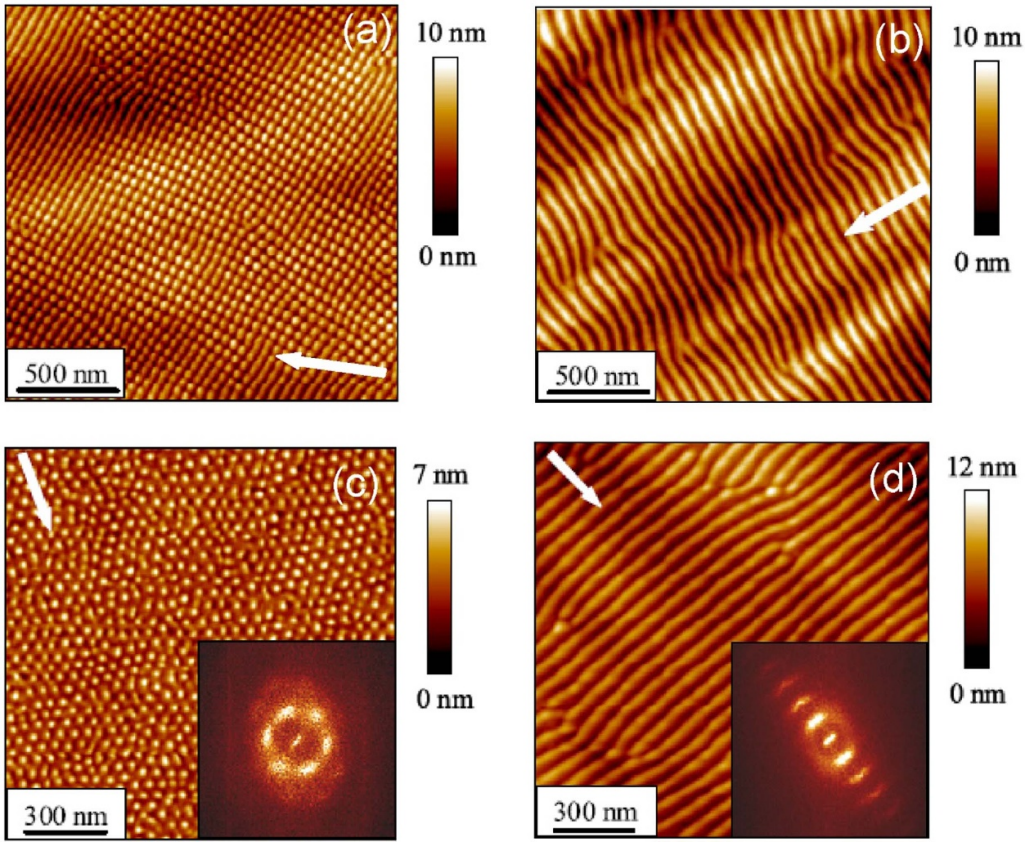

Figure 23. (a) AFM image of a Si surface irradiated by 1.2 keV Xe^+ impinging at 26°; (b) AFM image of a Si surface irradiated by 1.2 keV Xe^+ impinging at 5°; (c) AFM image of a Ge surface irradiated by Xe^+ impinging at 20°. (d) AFM image of a Ge surface irradiated by Xe^+ impinging at 5°. The arrows indicate the ion beam direction. Insets: corresponding FFT images. Reproduced from [231].

beam ion source. At that time, the authors of these reports were not aware of metal incorporation during IBI. Later, Cornejo *et al* [86] detailed how the operational parameters of the ion source may affect the ion divergence. For some conditions the divergence is so great that some parts of the chamber can be hit by the ion beam leading to unnoticed Fe co-deposition on the target surface. Thus, the ion beam divergence and its dependence on some operational parameters, particularly the acceleration voltage in this set-up, are behind the striking patterns obtained with these systems.

Although the specific conditions required by the above results in order to be reproduced in other IBI systems in a controlled way, are unknown, the results indeed show the high degree of order that can be achieved in the ripple and dot patterns when IBI with metal co-deposition is employed. Therefore, these results are a strong motivation to pursue the understanding of such ordering, both from the theoretical and the experimental points of view. Issues to be addressed include the influence of the target/impurity combination on the pattern ordering [121]. As figure 15 shows, Mo seeding seems to lead to more ordered patterns than Fe seeding. In addition, the ion energy and species, can affect also the pattern ordering seen in experiments with medium-energy ions [126]. Another pattern ordering feature characteristic of IBI with co-deposition, which contrasts with IBI without compositional effects, is that order may increase with ion fluence [108, 112, 205]. Finally, the target temperature is another parameter whose influence on the pattern ordering has not been addressed. Therefore, we think that there is room for further research in the field, by studying systematically the mechanisms behind the enhanced pattern ordering in IBI with metal co-deposition. In this line, the controlled design of novel experimental set-ups as such reported by Zhang *et al* [234] could contribute to achieve enhanced order or new surface patterns.

6.2. Chemical patterning

Another interesting feature of IBI patterning with concurrent atom co-deposition is the possibility to produce a chemical pattern alongside with the morphological one. This feature is not only observed experimentally, but also predicted theoretically [103, 104]. As we have seen in section 3, chemical patterns with different correlation with the morphological one can be obtained by co-depositing directionally Fe atoms or bombarding with Fe^+ ions a silicon target. The chemical patterning ultimately depends on the reaction of the incoming ion with the target atoms to form a compound with a lower SY than that of the target atoms, or in the co-deposition of atoms that react with those of the target. In this way, the zones rich in this compound will lead to a surface instability that will develop

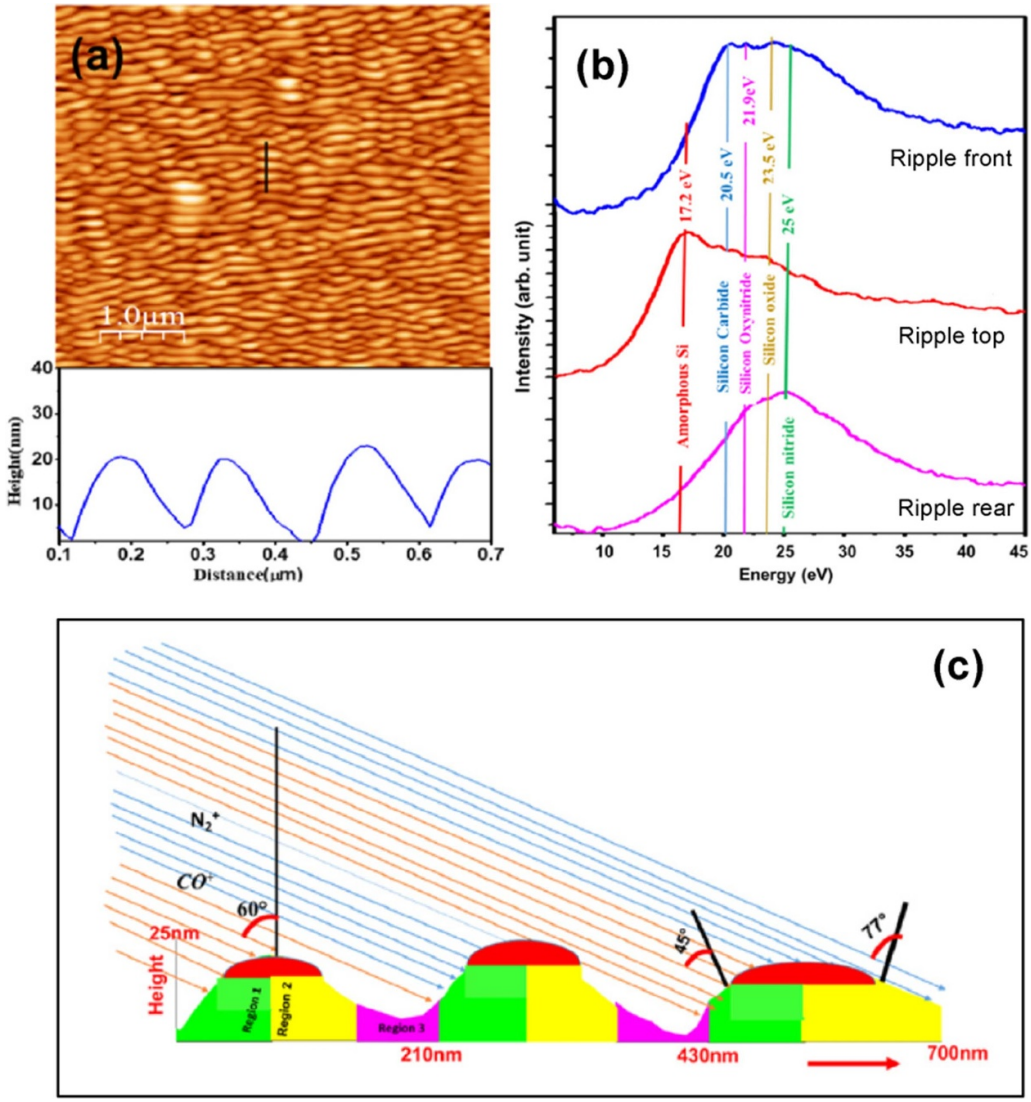

Figure 24. (a) Top: AFM image of a Si surface bombarded at 60° with 14 keV mixed CO^+ and N_2^+ ion beam at a fluence of 3×10^{17} ions cm^{-2}; bottom: surface profile along the line depicted in the AFM image. (b) EELS spectra taken at different ripple locations. (c) Scheme of the morphological and chemical phase patterns induced by the mixed IBI at a fluence of 3×10^{17} ions cm^{-2}. Note the colour code for each region: green (mixture of silicon carbide, silicon oxide, silicon nitride and silicon oxynitride), yellow (mixture of silicon oxide, silicon nitride and silicon oxynitride) and purple (amorphous silicon). Reproduced from [237].

with fluence and also would enhance the heterogeneity of the surface compound distribution.

The decisive role of the ion induced chemistry on the surface patterning was shown by Karmakar and Satpati when they were able to produce a ripple patterning on Si and Ge surfaces with a N^+ beam under conditions where no pattern was induced using an Ar^+ beam [235]. This concept was further employed to generate a chemical pattern on a Si surface using a NO^+ ion beam impacting at oblique incidence. A ripple pattern forms with alternate silicon oxy-nitride and silicon oxide enriched sites, when the NO^+ ion-induced chemistry operates under oblique ion incidence, together with geometrical shadowing effects. This occurs due to the fact that at high fluence the amplitude of the ripples increases and eventually a saw-tooth morphology forms. At this stage, the NO^+ ion beam impinges mainly on the upwind sides facing the incoming beam, which become silicon oxy-nitride-rich, while the downwind sides are shadowed from the incoming ion beam and remain silicon oxide-rich. These chemical and morphological patterns develop as a consequence of the interplay of the dissimilar chemical reactivity of oxygen and nitrogen with silicon, slope-dependent ion implantation, unequal SR of elemental silicon, silicon oxide, oxy-nitride and nitride, and the beam shadowing effect [236]. These concepts were further employed for irradiating a Si surface with a mixed (CO^+ and N_2^+) ion beam at $\theta = 60°$. The bombardment with three reactive ions, namely carbon, oxygen and nitrogen, leads to a ripple pattern and to the formation of spatially varying periodic chemical phases [237]. The composition of the chemical pattern was determined by XPS, STEM-high angle annual dark field and EELS. Examples of the results of this study are shown in figure 24, where the ripple morphological pattern is evident.

In addition, the EELS spectra, taken at different locations of the ripple nanostructure, show the contributions of each chemical phase in each case. Finally, figure 24(c) is a scheme of both, morphological and chemical, patterns proposed by the authors.

It is important to note that already from the first years of this century Smirnov *et al* [147] proposed to use IBI induced chemical patterns as selective doping implantation barriers with applications in the metal-oxide-semiconductor technology.

7. Conclusions

We have reviewed recent progress in the understanding and production of surface nano-patterns by IBI when compositional effects are relevant. Two main systems have been considered, namely, compound target surfaces and mono-elemental surfaces onto which foreign atoms are supplied concurrently to the irradiation, either via co-deposition or supplied by the ion beam itself. In the second main systems a compound is usually formed during IBI due to the reaction of the foreign (e.g. metal) atoms with the target ones (e.g. Si). For all the systems considered, we have detailed how, in addition to the mechanisms operating on IBI of mono-elemental surfaces without compositional heterogeneity, the surface diffusivities and SY of the different elements or compounds play relevant roles on the pattern formation, development, and properties.

With regard to the case of IBI with concurrent metal co-deposition, we have highlighted how the experimental set-up determines the pattern properties in this approach to surface nanostructuring. This fact explains the contradicting reports at the beginning of this century that delayed the understanding of the main operating mechanisms. Nevertheless, further controlled experiments are still needed to deepen the understanding of the mechanisms behind the enhanced order that these patterns can display, as compared to those patterns produced on compositionally homogeneous surfaces. This issue also requires additional well-controlled experiments and detailed and systematic theoretical modelling. Moreover, the possibility to produce both morphological and chemical patterns, with different correlation between them, has to be further explored, as it may be exploited for novel applications. In addition, the fact that the induced patterns depend to a great extent on the specific set-up geometry opens the possibility to look for new arrangements that lead to new or improved morphological structures. Also, the fact that the use of medium-energy ions produces nanostructures, particularly dots, with higher aspect ratios can be explored. We have discussed some reports that remain somewhat contradictory, in particular those which employ gold as the foreign atom. We think that a deeper study of the dependence of pattern properties on IBI parameters when using this foreign atom deserves further attention. From the theoretical point of view, the results obtained for the main models proposed so far are mostly within linear approximations. Therefore, they address the early stages of the pattern development. Further research is needed that considers the long time evolution of these patterns by assessing non-linear effects. For all these reasons, it is worth continuing research on the topic of this review since important issues still remain to be addressed.

Data availability statement

The data that support the findings of this study are available upon reasonable request from the authors.

Acknowledgments

We want to thank our close colleagues with whom we have shared research on IBI nanopatterning during the past years: R Gago, M Castro, J Muñoz-García, A Moreno-Barrado, J A Sánchez-García, C Ballesteros, B Galiana, M Varela, R Hübner, and J-S Kim. Particularly, we are indebted to R Gago for producing some of the patterns shown in this review. This work was supported by Ministerio de Economía, Industria y Competitividad (MINECO, Spain), Agencia Estatal de Investigación (AEI, Spain), and Fondo Europeo de Desarrollo Regional (FEDER, EU) through Grant No. PGC2018-094763-B-I00, and by Comunidad de Madrid (Spain) under the Multiannual Agreement with UC3M in the line of Excellence of University Professors, No. EPUC3M23, in the context of the V Plan Regional de Investigación Científica e Innovación Tecnológica (PRICIT), as well as under the TRANSNANOAVANSENS program (S2018-NMT-4349).

ORCID iDs

L Vázquez https://orcid.org/0000-0001-6220-2810
A Redondo-Cubero https://orcid.org/0000-0002-9981-6645
K Lorenz https://orcid.org/0000-0001-5546-6922
F J Palomares https://orcid.org/0000-0002-4768-2219
R Cuerno https://orcid.org/0000-0002-3563-771X

References

[1] Cunningham R L, Haymann P, Lecomte C, Moore W J and Trillat J J 1960 Etching of surfaces with 8-keV argon ions *J. Appl. Phys.* **31** 839–42
[2] Navez M, Chaperot D and Sella C 1962 Microscopie electronique-etude de lattaque du verre par bombardement ionique *C. R. Hebd. Seances Acad. Sci.* **254** 240
[3] Taniguchi N 1974 On the basic concept of nano-technology *Proc. Int. Conf. Production Engineering* (Tokyo: Japan Society of Precision Engineering) pp 18–23
[4] Valbusa U, Boragno C and de Mongeot F B 2002 Nanostructuring surfaces by ion sputtering *J. Phys.: Condens. Matter* **14** 8153–75
[5] Chan W L and Chason E 2007 Making waves: kinetic processes controlling surface evolution during low energy ion sputtering *J. Appl. Phys.* **101** 1
[6] Muñoz-García J, Vázquez L, Castro M, Gago R, Redondo-Cubero A, Moreno-Barrado A and Cuerno R 2014 Self-organized nanopatterning of silicon surfaces by ion beam sputtering *Mater. Sci. Eng. R Rep.* **86** 1–44
[7] Kang M and Goldman R 2019 Ion irradiation of III–V semiconductor surfaces: from self-assembled

nanostructures to plasmonic crystals *Appl. Phys. Rev.* **6** 041307
[8] Kim J, Ha N, Kim J, Joe M, Lee K and Cuerno R 2011 One-dimensional pattern of Au nanodots by ion-beam sputtering: formation and mechanism *Nanotechnology* **22** 285301
[9] Facsko S, Dekorsy T, Koerdt C, Trappe C, Kurz H, Vogt A and Hartnagel H L 1999 Formation of ordered nanoscale semiconductor dots by ion sputtering *Science* **285** 1551–3
[10] Carbone D, Biermanns A, Ziberi B, Frost F, Plantevin O, Pietsch U and Metzger T 2009 Ion-induced nanopatterns on semiconductor surfaces investigated by grazing incidence x-ray scattering techniques *J. Phys.: Condens. Matter* **21** 224007
[11] Castro M, Gago R, Vázquez L, Muñoz-García J and Cuerno R 2012 Stress-induced solid flow drives surface nanopatterning of silicon by ion-beam irradiation *Phys. Rev.* B **86** 214107
[12] Teichmann M, Lorbeer J, Ziberi B, Frost F and Rauschenbach B 2013 Pattern formation on Ge by low energy ion beam erosion *New J. Phys.* **15** 103029
[13] Engler M, Frost F, Müller S, Macko S, Will M, Feder R, Spemann D, Hübner R, Facsko S and Michely T 2014 Silicide induced ion beam patterning of Si(001) *Nanotechnology* **25** 115303
[14] Chowdhury D, Ghose D, Mollick S A, Satpati B and Bhattacharyya S R 2015 Nanorippling of ion irradiated GaAs (001) surface near the sputter-threshold energy *Phys. Status Solidi* b **252** 811–5
[15] El-Atwani O, Norris S, Ludwig K, Gonderman S and Allain J 2015 Ion beam nanopatterning of III–V semiconductors: consistency of experimental and simulation trends within a chemistry-driven theory *Sci. Rep.* **5** 18207
[16] Trynkiewicz E, Jany B, Janas A and Krok F 2018 Recent developments in ion beam-induced nanostructures on AIII-BV compound semiconductors *J. Phys.: Condens. Matter* **30** 304005
[17] Luttrell T and Batzill M 2010 Nanoripple formation on TiO_2 (110) by low-energy grazing incidence ion sputtering *Phys. Rev.* B **82** 035408
[18] Redondo-Cubero A, Vázquez L, Jalabert D, Lorenz K and Ben Sedrine N 2019 Modelling of optical damage in nanorippled ZnO produced by ion irradiation *Crystals* **9** 453
[19] Mussi V, Granone F, Boragno C, Buatier de Mongeot F, Valbusa U, Marolo T and Montereali R 2006 Surface nanostructuring and optical activation of lithium fluoride crystals by ion beam irradiation *Appl. Phys. Lett.* **88** 103116
[20] Krok F, Saeed S, Postawa Z and Szymonski M 2009 Ballistic versus electronic processes in ion-induced nanostructuring of ionic surfaces *Phys. Rev.* B **79** 235432
[21] Moon M-W, Han J H, Vaziri A, Her E K, Oh K H, Lee K-R and Hutchinson J W 2009 Nanoscale ripples on polymers created by a focused ion beam *Nanotechnology* **20** 115301
[22] Goyal M, Aggarwal S, Sharma A and Ojha S 2018 Surface structuring in polypropylene using Ar^+ beam sputtering: pattern transition from ripples to dot nanostructures *Appl. Surf. Sci.* **439** 380–5
[23] Arias S L, Cheng M K, Civantos A, Devorkin J, Jaramillo C and Allain J P 2020 Ion-induced nanopatterning of bacterial cellulose hydrogels for biosensing and anti-biofouling interfaces *ACS Appl. Nano Mater.* **3** 6719–28
[24] Teichert C 2003 Self-organized semiconductor surfaces as templates for nanostructured magnetic thin films *Appl. Phys.* A **76** 653–64
[25] Chen Y and Wang J-P 2004 Manufacturing method for high-density magnetic data storage media US 6719841
[26] de Miguel J, Bobek T and Teichert C 2011 Recent patents on self-organised magnetic nanodot arrays *Recent Pat. Nanotechnol.* **5** 1–18
[27] Arranz M A, Colino J M and Palomares F J 2014 On the limits of uniaxial magnetic anisotropy tuning by a ripple surface pattern *J. Appl. Phys.* **115** 183906
[28] Arranz M A and Colino J M 2015 Angular tuning of the magnetic birefringence in rippled cobalt films *Appl. Phys. Lett.* **106** 253102
[29] Oates T W, Keller A, Facsko S and Mücklich A 2007 Aligned silver nanoparticles on rippled silicon templates exhibiting anisotropic plasmon absorption *Plasmonics* **2** 47–50
[30] Ou X, Kögler R, Wei X, Mücklich A, Wang X, Skorupa W and Facsko S 2011 Fabrication of horizontal silicon nanowire arrays on insulator by ion irradiation *AIP Adv.* **1** 042174
[31] Chiappe D, Toma A and de Mongeot F B 2013 Transparent plasmonic nanowire electrodes via self-organised ion beam nanopatterning *Small* **9** 913–9
[32] Mennucci C, Muhammad M, Hameed M F O, Mohamed S A, Abdelkhalik M S, Obayya S and de Mongeot F B 2018 Broadband light trapping in nanotextured thin film photovoltaic devices *Appl. Surf. Sci.* **446** 74–82
[33] Yang Y and Keller A 2021 Ion beam nanopatterning of biomaterial surfaces *Appl. Sci.* **11** 6575
[34] Repetto D, Giordano M C, Foti A, Gucciardi P G, Mennucci C and de Mongeot F B 2018 SERS amplification by ultra-dense plasmonic arrays on self-organized PDMS templates *Appl. Surf. Sci.* **446** 83–91
[35] Sooraj K, Ranjan M, Rao R and Mukherjee S 2018 SERS based detection of glucose with lower concentration than blood glucose level using plasmonic nanoparticle arrays *Appl. Surf. Sci.* **447** 576–81
[36] Barelli M, Giordano M C, Gucciardi P G and Buatier de Mongeot F 2020 Self-organized nanogratings for large-area surface plasmon polariton excitation and surface-enhanced Raman spectroscopy sensing *ACS Appl. Nano Mater.* **3** 8784–93
[37] Augustine S, Sooraj K, Pachchigar V, Krishna C M and Ranjan M 2021 SERS based detection of Dichlorvos pesticide using silver nanoparticles arrays: influence of array wavelength/amplitude *Appl. Surf. Sci.* **544** 148878
[38] Chason E and Chan W 2009 Kinetic Monte Carlo simulations compared with continuum models and experimental properties of pattern formation during ion beam sputtering *J. Phys.: Condens. Matter* **21** 224016
[39] Norris S A and Aziz M J 2019 Ion-induced nanopatterning of silicon: toward a predictive model *Appl. Phys. Rev.* **6** 011311
[40] Cuerno R and Kim J-S 2020 A perspective on nanoscale pattern formation at surfaces by ion-beam irradiation *J. Appl. Phys.* **128** 180902
[41] Sigmund P 1969 Theory of sputtering. I. Sputtering yield of amorphous and polycrystalline targets *Phys. Rev.* **184** 383
[42] Sigmund P 1973 A mechanism of surface micro-roughening by ion bombardment *J. Mater. Sci.* **8** 1545–53
[43] Bradley R M and Harper J M E 1988 Theory of ripple topography induced by ion bombardment *J. Vac. Sci. Technol.* A **6** 2390–5
[44] Cuerno R and Barabási A-L 1995 Dynamic scaling of ion-sputtered surfaces *Phys. Rev. Lett.* **74** 4746
[45] Makeev M A, Cuerno R and Barabasi A-L 2002 Morphology of ion-sputtered surfaces *Nucl. Instrum. Methods Phys. Res.* B **197** 185–227
[46] Carter G and Vishnyakov V 1996 Roughening and ripple instabilities on ion-bombarded Si *Phys. Rev.* B **54** 17647

[47] Umbach C C, Headrick R L and Chang K-C 2001 Spontaneous nanoscale corrugation of ion-eroded SiO_2: the role of ion-irradiation-enhanced viscous flow *Phys. Rev. Lett.* **87** 246104

[48] Norris S A 2012 Stress-induced patterns in ion-irradiated silicon: model based on anisotropic plastic flow *Phys. Rev.* B **86** 235405

[49] Muñoz-García J, Cuerno R and Castro M 2019 Stress-driven nonlinear dynamics of ion-induced surface nanopatterns *Phys. Rev.* B **100** 205421

[50] Castro M and Cuerno R 2012 Hydrodynamic approach to surface pattern formation by ion beams *Appl. Surf. Sci.* **258** 4171–8

[51] Hofsäss H, Zhang K and Bobes O 2016 Self-organized surface ripple pattern formation by ion implantation *J. Appl. Phys.* **120** 135308

[52] Bradley R M and Hofsäss H 2016 Nanoscale patterns produced by self-sputtering of solid surfaces: the effect of ion implantation *J. Appl. Phys.* **120** 074302

[53] Hofsäss H and Bobes O 2019 Prediction of ion-induced nanopattern formation using Monte Carlo simulations and comparison to experiments *Appl. Phys. Rev.* **6** 021307

[54] Loew K M and Bradley R M 2019 Effect of dispersion on the nanoscale patterns produced by ion sputtering *Phys. Rev.* E **100** 012801

[55] Wendler E, Wesch W, Azarov A Y, Catarino N, Redondo-Cubero A, Alves E and Lorenz K 2013 Comparison of low-and room-temperature damage formation in Ar ion implanted GaN and ZnO *Nucl. Instrum. Methods Phys. Res.* B **307** 394–8

[56] Lorenz K, Wendler E, Redondo-Cubero A, Catarino N, Chauvat M-P, Schwaiger S, Scholz F, Alves E and Ruterana P 2017 Implantation damage formation in a-, c- and m-plane GaN *Acta Mater.* **123** 177–87

[57] Gago R, Vázquez L, Palomares F J, Agulló-Rueda F, Vinnichenko M, Carcelén V, Olvera J, Plaza J and Diéguez E 2013 Self-organized surface nanopatterns on Cd (Zn) Te crystals induced by medium-energy ion beam sputtering *J. Phys. Appl. Phys.* **46** 455302

[58] Chason E, Mayer T, Kellerman B, McIlroy D and Howard A 1994 Roughening instability and evolution of the Ge (001) surface during ion sputtering *Phys. Rev. Lett.* **72** 3040

[59] MacLaren S, Baker J, Finnegan N and Loxton C 1992 Surface roughness development during sputtering of GaAs and InP: evidence for the role of surface diffusion in ripple formation and sputter cone development *J. Vac. Sci. Technol.* A **10** 468–76

[60] Karen A, Okuno K, Soeda F and Ishitani A 1991 A study of the secondary-ion yield change on the GaAs surface caused by the O_2^+ ion-beam-induced rippling *J. Vac. Sci. Technol.* A **9** 2247–52

[61] Demanet C, Malherbe J, Van der Berg N and Sankar V 1995 Atomic force microscopy investigation of argon-bombarded InP: effect of ion dose density *Surf. Interface Anal.* **23** 433–9

[62] Mayer T, Chason E and Howard A 1994 Roughening instability and ion-induced viscous relaxation of SiO_2 surfaces *J. Appl. Phys.* **76** 1633–43

[63] Gago R, Vázquez L, Cuerno R, Varela M, Ballesteros C and Albella J M 2001 Production of ordered silicon nanocrystals by low-energy ion sputtering *Appl. Phys. Lett.* **78** 3316–8

[64] Cuenat A and Aziz M J 2001 Spontaneous pattern formation from focused and unfocused ion beam irradiation *MRS Online Proc. Libr. OPL* **696** 28

[65] Ludwig F Jr, Eddy C Jr, Malis O and Headrick R 2002 Si (100) surface morphology evolution during normal-incidence sputtering with 100–500 eV Ar^+ ions *Appl. Phys. Lett.* **81** 2770–2

[66] Ling L, Li W, Qi L, Lu M, Yang X and Gu C 2005 Nanopatterning of Si (110) surface by ion sputtering: an experimental and simulation study *Phys. Rev.* B **71** 155329

[67] Ziberi B, Frost F, Rauschenbach B and Höche T 2005 Highly ordered self-organized dot patterns on Si surfaces by low-energy ion-beam erosion *Appl. Phys. Lett.* **87** 033113

[68] Fan W, Li W, Qi L, Sun H, Luo J, Zhao Y and Lu M 2005 On the role of ion flux in nanostructuring by ion sputter erosion *Nanotechnology* **16** 1526

[69] Lu M, Yang X, Perry S and Rabalais J 2002 Self-organized nanodot formation on MgO (100) by ion bombardment at high temperatures *Appl. Phys. Lett.* **80** 2096–8

[70] Ziberi B, Frost F, Tartz M, Neumann H and Rauschenbach B 2004 Importance of ion beam parameters on self-organized pattern formation on semiconductor surfaces by ion beam erosion *Thin Solid Films* **459** 106–10

[71] Kahng B, Jeong H and Barabási A-L 2001 Quantum dot and hole formation in sputter erosion *Appl. Phys. Lett.* **78** 805–7

[72] Bobek T, Facsko S, Kurz H, Dekorsy T, Xu M and Teichert C 2003 Temporal evolution of dot patterns during ion sputtering *Phys. Rev.* B **68** 085324

[73] Facsko S, Bobek T, Stahl A, Kurz H and Dekorsy T 2004 Dissipative continuum model for self-organized pattern formation during ion-beam erosion *Phys. Rev.* B **69** 153412

[74] Kim T *et al* 2004 Kinetic roughening of ion-sputtered Pd (001) surface: beyond the Kuramoto–Sivashinsky model *Phys. Rev. Lett.* **92** 246104

[75] Castro M and Cuerno R 2005 Comment on 'Kinetic roughening of ion-sputtered Pd (001) surface: beyond the Kuramoto–Sivashinsky model' *Phys. Rev. Lett.* **94** 139601

[76] Kim T 2005 Kim et al. Reply *Phys. Rev. Lett.* **94** 139602

[77] Castro M, Cuerno R, Vázquez L and Gago R 2005 Self-organized ordering of nanostructures produced by ion-beam sputtering *Phys. Rev. Lett.* **94** 016102

[78] Vogel S and Linz S J 2005 Continuum modeling of sputter erosion under normal incidence: interplay between nonlocality and nonlinearity *Phys. Rev.* B **72** 035416

[79] Ozaydin G, Özcan A S, Wang Y, Ludwig K F, Zhou H, Headrick R L and Siddons D P 2005 Real-time x-ray studies of Mo-seeded Si nanodot formation during ion bombardment *Appl. Phys. Lett.* **87** 163104

[80] Teichert C, Hofer C and Hlawacek G 2006 Self-organization of nanostructures in inorganic and organic semiconductor systems *Adv. Eng. Mater.* **8** 1057–65

[81] Madi C S, Davidovitch B, George H B, Norris S A, Brenner M P and Aziz M J 2008 Multiple bifurcation types and the linear dynamics of ion sputtered surfaces *Phys. Rev. Lett.* **101** 246102

[82] Madi C S, George H B and Aziz M J 2009 Linear stability and instability patterns in ion-sputtered silicon *J. Phys.: Condens. Matter* **21** 224010

[83] Bhowmik D, Mukherjee M and Karmakar P 2019 Presence of reactive impurities in Ar^+ ion beam plays a key role for Si ripple formation *Nucl. Instrum. Methods Phys. Res.* B **444** 54–61

[84] Ozaydin-Ince G and Ludwig Jr K 2009 *In situ* x-ray studies of native and Mo-seeded surface nanostructuring during ion bombardment of Si (100) *J. Phys.: Condens. Matter* **21** 224008

[85] Macko S, Frost F, Ziberi B, Förster D F and Michely T 2010 Is keV ion-induced pattern formation on Si(001) caused by metal impurities? *Nanotechnology* **21** 085301

[86] Cornejo M, Ziberi B, Meinecke C, Hirsch D, Gerlach J W, Höche T, Frost F and Rauschenbach B 2011 Self-organized patterning on Si(001) by ion sputtering with simultaneous metal incorporation *Appl. Phys.* A **102** 593–9

[87] Zhou J, Facsko S, Lu M and Möller W 2011 Nanopatterning of Si surfaces by normal incident ion erosion: influence of iron incorporation on surface morphology evolution *J. Appl. Phys.* **109** 104315

[88] Madi C S and Aziz M J 2012 Multiple scattering causes the low energy–low angle constant wavelength topographical instability of argon ion bombarded silicon surfaces *Appl. Surf. Sci.* **258** 4112–5

[89] Gnaser H 2011 Nanostructures on surfaces by ion irradiation *Pure Appl. Chem.* **83** 2003–25

[90] Hofsäss H and Zhang K 2008 Surfactant sputtering *Appl. Phys.* A **92** 517–24

[91] Gnaser H 1999 *Low-Energy Ion Irradiation of Solid Surfaces* vol 146 (Berlin: Springer)

[92] Moreno-Barrado A, Castro M, Gago R, Vázquez L, Muñoz-García J, Redondo-Cubero A, Galiana B, Ballesteros C and Cuerno R 2015 Nonuniversality due to inhomogeneous stress in semiconductor surface nanopatterning by low-energy ion-beam irradiation *Phys. Rev.* B **91** 155303

[93] Moreno-Barrado A, Gago R, Redondo-Cubero A, Vázquez L, Muñoz-García J, Cuerno R, Lorenz K and Castro M 2015 Ion damage overrides structural disorder in silicon surface nanopatterning by low-energy ion beam sputtering *Europhys. Lett.* **109** 48003

[94] Kumar T, Kumar A and Kanjilal D 2013 An approach to tune the amplitude of surface ripple patterns *Appl. Phys. Lett.* **103** 131604

[95] Kumar T, Kumar A, Agarwal D C, Lalla N P and Kanjilal D 2013 Ion beam-generated surface ripples: new insight in the underlying mechanism *Nanoscale Res. Lett.* **8** 336

[96] Kumar T, Kumar M, Panchal V, Sahoo P and Kanjilal D 2015 Energy-separated sequential irradiation for ripple pattern tailoring on silicon surfaces *Appl. Surf. Sci.* **357** 184–8

[97] Panchal V, Kumar T, Satpati B, Ojha S and Kumar S 2020 Evaluation of the effect of low fluence ion beam pre-damage with sequential high fluence ion beam exposure on the characteristics of the resultant surface *Surf. Interfaces* **18** 100425

[98] Ou X, Heinig K-H, Hübner R, Grenzer J, Wang X, Helm M, Fassbender J and Facsko S 2015 Faceted nanostructure arrays with extreme regularity by self-assembly of vacancies *Nanoscale* **7** 18928–35

[99] Erlebacher J, Aziz M J, Chason E, Sinclair M B and Floro J A 1999 Spontaneous pattern formation on ion bombarded Si(001) *Phys. Rev. Lett.* **82** 2330

[100] Brown A-D and Erlebacher J 2005 Temperature and fluence effects on the evolution of regular surface morphologies on ion-sputtered Si (111) *Phys. Rev.* B **72** 075350

[101] Hofsäss H, Zhang K and Mutzke A 2014 Simulation of ion beam sputtering with SDTrimSP, TRIDYN and SRIM *Appl. Surf. Sci.* **310** 134–41

[102] Norris S A, Perkinson J C, Mokhtarzadeh M, Anzenberg E, Aziz M J and Ludwig K F 2017 Distinguishing physical mechanisms using GISAXS experiments and linear theory: the importance of high wavenumbers *Sci. Rep.* **7** 2016

[103] Shenoy V, Chan W and Chason E 2007 Compositionally modulated ripples induced by sputtering of alloy surfaces *Phys. Rev. Lett.* **98** 256101

[104] Bradley R M 2013 Nanoscale patterns produced by ion erosion of a solid with codeposition of impurities: the crucial effect of compound formation *Phys. Rev.* B **87** 205408

[105] Ozaydin G, Ludwig J K F, Zhou H and Headrick R L 2008 Effects of Mo seeding on the formation of Si nanodots during low-energy ion bombardment *J. Vac. Sci. Technol.* B **26** 551–8

[106] Cuenat A, George H B, Chang K, Blakely J M and Aziz M J 2005 Lateral templating for guided self-organization of sputter morphologies *Adv. Mater.* **17** 2845–9

[107] Keller A, Facsko S and Möller W 2008 Minimization of topological defects in ion-induced ripple patterns on silicon *New J. Phys.* **10** 063004

[108] Redondo-Cubero A, Palomares F J, Hübner R, Gago R and Vázquez L 2020 Highly ordered silicide ripple patterns induced by medium-energy ion irradiation *Phys. Rev.* B **102** 075423

[109] Redondo-Cubero A, Lorenz K, Palomares F J, Muñoz A, Castro M, Muñoz-García J, Cuerno R and Vázquez L 2018 Concurrent segregation and erosion effects in medium-energy iron beam patterning of silicon surfaces *J. Phys.: Condens. Matter* **30** 274001

[110] Xin Y, Martinez Rivadeneira S, Grundmeier G, Castro M and Keller A 2020 Self-assembly of highly ordered DNA origami lattices at solid-liquid interfaces by controlling cation binding and exchange *Nano Res.* **13** 3142–50

[111] Barabási A-L and Stanley H E 1995 *Fractal Concepts in Surface Growth* (Cambridge: Cambridge University Press)

[112] Zhang K, Brötzmann M and Hofsäss H 2011 Surfactant-driven self-organized surface patterns by ion beam erosion *New J. Phys.* **13** 013033

[113] Macko S, Frost F, Engler M, Hirsch D, Höche T, Grenzer J and Michely T 2011 Phenomenology of iron-assisted ion beam pattern formation on Si(001) *New J. Phys.* **13** 073017

[114] Hofsäss H, Zhang K, Pape A, Bobes O and Brötzmann M 2013 The role of phase separation for self-organized surface pattern formation by ion beam erosion and metal atom co-deposition *Appl. Phys.* A **111** 653–64

[115] Zhang K, Brötzmann M and Hofsäss H 2012 Sharp transition from ripple patterns to a flat surface for ion beam erosion of Si with simultaneous co-deposition of iron *AIP Adv.* **2** 032123

[116] Koyiloth Vayalil S, Gupta A and Roth S V 2017 Study of pattern transition in nanopatterned Si (100) produced by impurity-assisted low-energy ion-beam erosion *Appl. Phys.* A **123** 225

[117] Sánchez-García J, Vázquez L, Gago R, Redondo-Cubero A, Albella J and Czigany Z 2008 Tuning the surface morphology in self-organized ion beam nanopatterning of Si(001) via metal incorporation: from holes to dots *Nanotechnology* **19** 355306

[118] Macko S, Grenzer J, Frost F, Engler M, Hirsch D, Fritzsche M, Mücklich A and Michely T 2012 Iron-assisted ion beam patterning of Si(001) in the crystalline regime *New J. Phys.* **14** 073003

[119] Bi Q, Chen Z, Liu Y, Tang L, Xi Y and Liu W 2020 Nanostructures on sapphire surfaces induced by metal impurity assisted ion beam *Coatings* **10** 949

[120] Redondo-Cubero A, Gago R, Palomares F J, Mücklich A, Vinnichenko M and Vázquez L 2012 Nanopatterning dynamics on Si(100) during oblique 40-keV Ar erosion with metal codeposition: morphological and compositional correlation *Phys. Rev.* B **86** 085436

[121] Gago R, Redondo-Cubero A, Palomares F J and Vázquez L 2014 Influence of metal co-deposition on silicon nanodot patterning dynamics during ion-beam sputtering *Nanotechnology* **25** 415301

[122] Ozaydin G, Özcan A S, Wang Y, Ludwig K F Jr, Zhou H and Headrick R L 2007 Real-time x-ray studies of the growth of Mo-seeded Si nanodots by low-energy ion bombardment *Nucl. Instrum. Methods Phys. Res.* B **264** 47–54

[123] Deka A, Barman P, Bhattacharjee G and Bhattacharyya S 2020 Evolution of ion-induced nano-dot patterns on

silicon surface in presence of seeding materials *Appl. Surf. Sci*. **526** 146645
[124] Muñoz-García J, Gago R, Vázquez L, Sánchez-García J A and Cuerno R 2010 Observation and modeling of interrupted pattern coarsening: surface nanostructuring by ion erosion *Phys. Rev. Lett.* **104** 026101
[125] Muñoz-García J, Gago R, Cuerno R, Sánchez-García J A, Redondo-Cubero A, Castro M and Vázquez L 2012 Independence of interrupted coarsening on initial system order: ion-beam nanopatterning of amorphous versus crystalline silicon targets *J. Phys.: Condens. Matter* **24** 375302
[126] Redondo-Cubero A, Galiana B, Lorenz K, Palomares F J, Bahena D, Ballesteros C, Hernandez-Calderón I and Vázquez L 2016 Self-organised silicide nanodot patterning by medium-energy ion beam sputtering of Si(100): local correlation between the morphology and metal content *Nanotechnology* **27** 444001
[127] Tocce E J, Smirnov V K, Kibalov D S, Liliensiek S J, Murphy C J and Nealey P F 2010 The ability of corneal epithelial cells to recognize high aspect ratio nanostructures *Biomaterials* **31** 4064–72
[128] Gago R, Vázquez L, Plantevin O, Sánchez-García J, Varela M, Ballesteros M, Albella J and Metzger T 2006 Temperature influence on the production of nanodot patterns by ion beam sputtering of Si(001) *Phys. Rev.* B **73** 155414
[129] Carter G, Nobes M and Katardjiev I 1988 Cone production on surfaces under congruent atomic deposition and ion bombardment *Vacuum* **38** 537–40
[130] Kaufman H R and Robinson R S 1979 Ion beam texturing of surfaces *J. Vac. Sci. Technol.* **16** 175–8
[131] Robinson R and Rossnagel S 1982 Ion-beam-induced topography and surface diffusion *J. Vac. Sci. Technol.* **21** 790–7
[132] Habenicht S, Lieb K, Koch J and Wieck A 2002 Ripple propagation and velocity dispersion on ion-beam-eroded silicon surfaces *Phys. Rev.* B **65** 115327
[133] Smirnova M, Ivanov A, Bachurin V and Churilov A 2021 Study of ripple formation on Si surface under Ga ion beam bombardment *J. Phys.: Conf. Ser.* **2086** 012210
[134] Adams D, Vasile M, Mayer T and Hodges V 2003 Focused ion beam milling of diamond: effects of H_2O on yield, surface morphology and microstructure *J. Vac. Sci. Technol.* B **21** 2334–43
[135] Fritzsche M, Muecklich A and Facsko S 2012 Nanohole pattern formation on germanium induced by focused ion beam and broad beam Ga^+ irradiation *Appl. Phys. Lett.* **100** 223108
[136] Böttger R, Heinig K-H, Bischoff L, Liedke B and Facsko S 2013 From holes to sponge at irradiated Ge surfaces with increasing ion energy—an effect of defect kinetics? *Appl. Phys.* A **113** 53–59
[137] Mayr S and Averback R S 2005 Ion-irradiation-induced stresses and swelling in amorphous Ge thin films *Phys. Rev.* B **71** 134102
[138] Swenson J M and Norris S A 2018 Swelling as a stabilizing mechanism in irradiated thin films *J. Phys.: Condens. Matter* **30** 304003
[139] Koukourinkova S D, Benamara M, Ware M E, Wang Z M and Salamo G J 2016 Formation of self-assembled Ga-rich droplet chains on GaAs (100) patterned by focused ion beam *Appl. Phys. Lett.* **109** 123102
[140] Mollick S A, Ghose D, Shipman P D and Mark Bradley R 2014 Anomalous patterns and nearly defect-free ripples produced by bombarding silicon and germanium with a beam of gold ions *Appl. Phys. Lett.* **104** 043103
[141] Mollick S A, Kumar M, Singh R, Satpati B, Ghose D and Som T 2016 Gold-decorated highly ordered self-organized grating-like nanostructures on Ge surface: Kelvin probe force microscopy and conductive atomic force microscopy studies *Nanotechnology* **27** 435302
[142] Dell'Anna R, Iacob E, Barozzi M, Vanzetti L, Hübner R, Böttger R, Giubertoni D and Pepponi G 2018 The role of incidence angle in the morphology evolution of Ge surfaces irradiated by medium-energy Au ions *J. Phys.: Condens. Matter* **30** 324001
[143] Fujiwara Y, Kondou K, Watanabe K, Nonaka H, Saito N, Itoh H, Fujimoto T, Kurokawa A, Ichimura S and Tomita M 2007 Beam-induced nanoscale ripple formation on silicon with the metal-cluster-complex ion of $Ir_4(CO)_7^+$ *Jpn. J. Appl. Phys*. **46** L854
[144] Liu Z and Alkemade P 2001 Flux dependence of oxygen-beam-induced ripple growth on silicon *Appl. Phys. Lett.* **79** 4334–6
[145] Homma Y, Takano A and Higashi Y 2003 Oxygen-ion-induced ripple formation on silicon: evidence for phase separation and tentative model *Appl. Surf. Sci.* **203** 35–38
[146] Gautier B, Fares B, Prudon G and Dupuy J-C 2004 Imaging by atomic force microscopy of the electrical properties difference of the facets of oxygen-ion-induced ripple topography in silicon *Appl. Surf. Sci.* **231** 136–40
[147] Smirnov V, Kibalov D, Orlov O and Graboshnikov V 2003 Technology for nanoperiodic doping of a metal–oxide–semiconductor field-effect transistor channel using a self-forming wave-ordered structure *Nanotechnology* **14** 709
[148] Karmakar P and Satpati B 2014 Site specific isolated nanostructure array formation on a large area by broad ion beam without any mask and resist *Appl. Phys. Lett.* **104** 231601
[149] Redondo-Cubero A, Palomares F, Lorenz K, Rubio-Zuazo J, Hübner R, Mompeán F, García-Hernández M, Castro G and Vázquez L 2022 Role of the metal supply pathway on silicon patterning by oblique ion beam sputtering *Appl. Surf. Sci.* **580** 152267
[150] Khanbabaee B, Lützenkirchen-Hecht D, Hübner R, Grenzer J, Facsko S and Pietsch U 2014 Near surface silicide formation after off-normal Fe-implantation of Si(001) surfaces *J. Appl. Phys.* **116** 024301
[151] Chini T K, Okuyama F, Tanemura M and Nordlund K 2003 Structural investigation of keV Ar-ion-induced surface ripples in Si by cross-sectional transmission electron microscopy *Phys. Rev.* B **67** 205403
[152] Datta D P and Chini T K 2004 Atomic force microscopy study of 60-keV Ar-ion-induced ripple patterns on Si(100) *Phys. Rev.* B **69** 235313
[153] Karmakar P and Ghose D 2005 Nanoscale periodic and faceted structures formation on Si(100) by oblique angle oxygen ion sputtering *Nucl. Instrum. Methods Phys. Res.* B **230** 539–44
[154] Basu T, Mohanty J R and Som T 2012 Unusual pattern formation on Si(100) due to low energy ion bombardment *Appl. Surf. Sci*. **258** 9944–8
[155] Basu T, Datta D P and Som T 2013 Transition from ripples to faceted structures under low-energy argon ion bombardment of silicon: understanding the role of shadowing and sputtering *Nanoscale Res. Lett.* **8** 289
[156] Chowdhury D and Ghose D 2015 Super-roughening scaling behaviour of Si surface morphology at grazing incidence low energy ion beam sputtering *Appl. Surf. Sci.* **324** 517–24
[157] Kumar P, Jain P and Sulania I 2016 Medium energy ion irradiation of Ge surface–search for a better understanding of the surface nano-patterning *Surf. Interface Anal.* **48** 196–201

[158] Datta D, Garg S, Basu T, Satpati B, Hofsäss H, Kanjilal D and Som T 2016 Temporal evolution of Ge surface topography under keV ion irradiation: combined effects of curvature-dependent sputter erosion and atomic redistribution *Appl. Surf. Sci.* **360** 131–42

[159] Chowdhury D and Ghose D 2017 Fabrication of nanoscale topographies on Ge(100) surface by low energy Ar^+ ion sputtering *Nucl. Instrum. Methods Phys. Res.* B **409** 197–201

[160] Flamm D, Frost F and Hirsch D 2001 Evolution of surface topography of fused silica by ion beam sputtering *Appl. Surf. Sci.* **179** 95–101

[161] Metya A, Ghose D, Mollick S and Majumdar A 2012 Nanopatterning of mica surface under low energy ion beam sputtering *J. Appl. Phys.* **111** 074306

[162] Adams D, Mayer T, Vasile M and Archuleta K 2006 Effects of evolving surface morphology on yield during focused ion beam milling of carbon *Appl. Surf. Sci.* **252** 2432–44

[163] Lee E, Seo J, Muñoz-García J, Castro M, Cuerno R and Kim J-S 2022 Nanopatterning of rotating highly oriented pyrolytic graphite (0001) surfaces by ion beam irradiation: experiments and modeling *Phys. Rev.* B **105** 085413

[164] Mishra P and Ghose D 2009 Effect of initial target surface roughness on the evolution of ripple topography induced by oxygen sputtering of Al films *J. Appl. Phys.* **105** 014304

[165] Pearson D A and Bradley R M 2014 Theory of terraced topographies produced by oblique-incidence ion bombardment of solid surfaces *J. Phys.: Condens. Matter* **27** 015010

[166] Harrison M P, Pearson D A and Bradley R M 2017 Emergence and detailed structure of terraced surfaces produced by oblique-incidence ion sputtering *Phys. Rev.* E **96** 032804

[167] Perkinson J C, Swenson J M, DeMasi A, Wagenbach C, Ludwig K F, Norris S A and Aziz M J 2018 Sawtooth structure formation under nonlinear-regime ion bombardment *J. Phys.: Condens. Matter* **30** 294004

[168] Karen A, Nakagawa Y, Hatada M, Okuno K, Soeda F and Ishitani A 1995 Quantitative investigation of the O_2^+-induced topography of GaAs and other III–V semiconductors: an STM study of the ripple formation and suppression of the secondary ion yield change by sample rotation *Surf. Interface Anal.* **23** 506–13

[169] Xu M and Teichert C 2005 Size distribution and dot shape of self-assembled quantum dots induced by ion sputtering *Physica* E **25** 425–30

[170] Allmers T, Donath M and Rangelov G 2006 Pattern formation by erosion sputtering on GaSb: transition from dot to ripple formation and influence of impurities *J. Vac. Sci. Technol.* B **24** 582–6

[171] Bobek T *et al* 2007 Self-organized hexagonal patterns of independent magnetic nanodots *Adv. Mater.* **19** 4375–80

[172] Kumar T, Khan S, Singh U, Verma S and Kanjilal D 2012 Formation of nanodots on GaAs by 50 keV Ar^+ ion irradiation *Appl. Surf. Sci.* **258** 4148–51

[173] Som T, Chini T, Katharia Y, Tripathy S and Kanjilal D 2009 Formation of nanodots on oblique ion sputtered InP surfaces *Appl. Surf. Sci.* **256** 562–6

[174] Katharria Y, Kumar S, Lakshmy P, Kanjilal D and Sharma A 2007 Self-organization of 6 H–Si C (0001) surface under keV ion irradiation *J. Appl. Phys.* **102** 044301

[175] Parida B, Ranjan M and Sarkar S 2018 Morphological instabilities in argon ion sputtered CoSi binary mixtures *Curr. Appl. Phys.* **18** 993–1000

[176] Parida B, Kundu A, Hazra K and Sarkar S 2021 Anisotropic electrical conduction on ion induced nanorippled CoSi surface *Appl. Phys.* A **127** 972

[177] Le Roy S, Barthel E, Brun N, Lelarge A and Søndergård E 2009 Self-sustained etch masking: a general concept to initiate the formation of nanopatterns during ion erosion *J. Appl. Phys.* **106** 094308

[178] Le Roy S, Søndergård E, Nerbø I, Kildemo M and Plapp M 2010 Diffuse-interface model for nanopatterning induced by self-sustained ion-etch masking *Phys. Rev.* B **81** 161401

[179] El-Atwani O, Allain J P and Suslova A 2012 The effect of native oxide on ion-sputtering-induced nanostructure formation on GaSb surfaces *Appl. Phys. Lett.* **101** 251606

[180] El-Atwani O, Allain J, Cimaroli A, Suslova A and Ortoleva S 2011 The significance of *in situ* conditions in the characterization of GaSb nanopatterned surfaces via ion beam sputtering *J. Appl. Phys.* **110** 074301

[181] Lively M A, Holybee B, Toriyama M, Facsko S and Allain J P 2020 Nonlinear compositional and morphological evolution of ion irradiated GaSb prior to nanostructure formation *Sci. Rep.* **10** 8253

[182] Chowdhury D and Ghose D 2019 Formation of nearly defect-free nanoripples by sputtering of GaAs (001) surface at high temperature *Surf. Interfaces* **17** 100364

[183] Huang Q, Feng J, Huang H, Yang X, Grenzer J, Huang K, Zhang S, Lin J, Zhou H and You T 2019 Realization of wafer-scale nanogratings with sub-50 nm period through vacancy epitaxy *Nat. Commun.* **10** 2437

[184] Wehner G and Hajicek D 1971 Cone formation on metal targets during sputtering *J. Appl. Phys.* **42** 1145–9

[185] Tanemura M, Kobayashi M, Kudo M, Yamauchi H, Okita T, Miao L and Tanemura S 2006 Fabrication of densely distributed Si nanorods by Ar^+-ion bombardment *Surf. Sci.* **600** 3668–72

[186] Shang N, Ma X, Liu C, Bello I and Lee S 2010 Arrays of Si cones prepared by ion beams: growth mechanisms *Phys. Status Solidi* a **207** 309–15

[187] Wilson I 1973 The topography of sputtered semiconductors *Radiat. Eff.* **18** 95–103

[188] Zhou J, Hildebrandt M and Lu M 2011 Self-organized antireflecting nano-cone arrays on Si (100) induced by ion bombardment *J. Appl. Phys.* **109** 053513

[189] Csepregi L, Kennedy E F, Mayer J and Sigmon T 1978 Substrate-orientation dependence of the epitaxial regrowth rate from Si-implanted amorphous Si *J. Appl. Phys.* **49** 3906–11

[190] Chowdhury D, Satpati B and Ghose D 2016 Temperature and high fluence induced ripple rotation on Si (100) surface *Mater. Res. Express* **3** 125003

[191] Ziegler J F, Biersack J P and Littmark U 1985 *The Stopping and Range of Ions in Matter* (New York: Pergamon)

[192] Sulania I, Agarwal D C, Kumar M, Kumar S and Kumar P 2016 Topography evolution of 500 keV Ar 4^+ ion beam irradiated InP (100) surfaces–formation of self-organized In-rich nano-dots and scaling laws *Phys. Chem. Chem. Phys.* **18** 20363–70

[193] Moroni E, Wolf W, Hafner J and Podloucky R 1999 Cohesive, structural, and electronic properties of Fe–Si compounds *Phys. Rev.* B **59** 12860

[194] Sánchez-García J, Gago R, Caillard R, Redondo-Cubero A, Martin-Gago J, Palomares F, Fernández M and Vázquez L 2009 Production of nanohole/nanodot patterns on Si(001) by ion beam sputtering with simultaneous metal incorporation *J. Phys.: Condens. Matter* **21** 224009

[195] Lloyd K S, Bolotin I L, Schmeling M, Hanley L and Veryovkin I V 2016 Metal impurity-assisted formation of nanocone arrays on Si by low energy ion-beam irradiation *Surf. Sci.* **652** 334–43

[196] Moon B, Yoo S, Kim J-S, Kang S J, Muñoz-García J and Cuerno R 2016 Ion-beam nanopatterning of silicon surfaces under codeposition of non-silicide-forming impurities *Phys. Rev.* B **93** 115430

[197] El-Atwani O, Ortoleva S, Cimaroli A and Allain J P 2011 Formation of silicon nanodots via ion beam sputtering of ultrathin gold thin film coatings on Si *Nanoscale Res. Lett.* **6** 403

[198] El-Atwani O, Suslova A, DeMasi A, Gonderman S, Fowler J, El-Atwani M, Ludwig K and Paul Allain J 2012 Real time x-ray studies during nanostructure formation on silicon via low energy ion beam irradiation using ultrathin iron films *Appl. Phys. Lett.* **101** 263104

[199] El-Atwani O, Gonderman S, DeMasi A, Suslova A, Fowler J, El-Atwani M, Ludwig K and Paul Allain J 2013 Nanopatterning of metal-coated silicon surfaces via ion beam irradiation: real time x-ray studies reveal the effect of silicide bonding *J. Appl. Phys.* **113** 124305

[200] Gago R, Jaafar M and Palomares F 2018 Surface morphology of molybdenum silicide films upon low-energy ion beam sputtering *J. Phys.: Condens. Matter* **30** 264003

[201] Möller W, Eckstein W and Biersack J 1988 Tridyn-binary collision simulation of atomic collisions and dynamic composition changes in solids *Comput. Phys. Commun.* **51** 355–68

[202] Eckstein W 1994 Backscattering and sputtering with the Monte-Carlo program TRIM.SP *Radiat. Eff. Defects Solids* **130** 239–50

[203] Bradley R M 2012 Producing ripple topographies by ion bombardment with codeposition of impurities: a curvature-dependent sputter yield is not required *Phys. Rev.* B **85** 115419

[204] Bradley R M 2016 Morphological transitions in nanoscale patterns produced by concurrent ion sputtering and impurity co-deposition *J. Appl. Phys.* **119** 134305

[205] Koyiloth Vayalil S, Gupta A, Roth S V and Ganesan V 2015 Investigation of the mechanism of impurity assisted nanoripple formation on Si induced by low energy ion beam erosion *J. Appl. Phys.* **117** 024309

[206] Feix M, Hartmann A, Kree R, Muñoz-García J and Cuerno R 2005 Influence of collision cascade statistics on pattern formation of ion-sputtered surfaces *Phys. Rev.* B **71** 125407

[207] Cross M and Greenside H 2009 *Pattern Formation and Dynamics in Nonequilibrium Systems* (Cambridge: Cambridge University Press)

[208] Aste T and Valbusa U 2004 Surface instabilities in granular matter and ion-sputtered surfaces *Physica* A **332** 548–58

[209] Csahók Z, Misbah C, Rioual F and Valance A 2000 Dynamics of aeolian sand ripples *Eur. Phys. J.* E **3** 71–86

[210] Muñoz-García J, Cuerno R and Castro M 2009 Coupling of morphology to surface transport in ion-beam-irradiated surfaces: normal incidence and rotating targets *J. Phys.: Condens. Matter* **21** 224020

[211] Muñoz-García J, Castro M and Cuerno R 2006 Nonlinear ripple dynamics on amorphous surfaces patterned by ion beam sputtering *Phys. Rev. Lett.* **96** 086101

[212] Muñoz-García J, Cuerno R and Castro M 2008 Coupling of morphology to surface transport in ion-beam irradiated surfaces: oblique incidence *Phys. Rev.* B **78** 205408

[213] Bradley R M and Shipman P D 2010 Spontaneous pattern formation induced by ion bombardment of binary compounds *Phys. Rev. Lett.* **105** 145501

[214] Shipman P D and Bradley R M 2011 Theory of nanoscale pattern formation induced by normal-incidence ion bombardment of binary compounds *Phys. Rev.* B **84** 085420

[215] Bradley R M and Shipman P D 2012 A surface layer of altered composition can play a key role in nanoscale pattern formation induced by ion bombardment *Appl. Surf. Sci.* **258** 4161–70

[216] Mark Bradley R 2012 Surface instability of binary compounds caused by sputter yield amplification *J. Appl. Phys.* **111** 114305

[217] Norris S A 2013 Ion-assisted phase separation in compound films: an alternate route to ordered nanostructures *J. Appl. Phys.* **114** 204303

[218] Motta F C, Shipman P D and Bradley R M 2012 Highly ordered nanoscale surface ripples produced by ion bombardment of binary compounds *J. Phys. Appl. Phys.* **45** 122001

[219] Kree R, Yasseri T and Hartmann A 2009 Surfactant sputtering: theory of a new method of surface nanostructuring by ion beams *Nucl. Instrum. Methods Phys. Res.* B **267** 1403–6

[220] Hartmann A K, Kree R and Yasseri T 2009 Simulating discrete models of pattern formation by ion beam sputtering *J. Phys.: Condens. Matter* **21** 224015

[221] Zhou J and Lu M 2010 Mechanism of Fe impurity motivated ion-nanopatterning of Si (100) surfaces *Phys. Rev.* B **82** 125404

[222] Bradley R M 2011 Theory of nanodot and sputter cone arrays produced by ion sputtering with concurrent deposition of impurities *Phys. Rev.* B **83** 195410

[223] Gago R, Vázquez L, Cuerno R, Varela M, Ballesteros C and Albella J M 2002 Nanopatterning of silicon surfaces by low-energy ion-beam sputtering: dependence on the angle of ion incidence *Nanotechnology* **13** 304

[224] Muñoz-García J, Cuerno R and Castro M 2006 Short-range stationary patterns and long-range disorder in an evolution equation for one-dimensional interfaces *Phys. Rev.* E **74** 050103

[225] Cuerno R, Makse H A, Tomassone S, Harrington S T and Stanley H E 1995 Stochastic model for surface erosion via ion sputtering: dynamical evolution from ripple morphology to rough morphology *Phys. Rev. Lett.* **75** 4464

[226] Keller A and Facsko S 2010 Tuning the quality of nanoscale ripple patterns by sequential ion-beam sputtering *Phys. Rev.* B **82** 155444

[227] Harrison M P and Bradley R M 2016 Producing virtually defect-free nanoscale ripples by ion bombardment of rocked solid surfaces *Phys. Rev.* E **93** 040802

[228] Jo S, Jun J, Lee E, Yoon S, Seo J, Muñoz-García J, Cuerno R and Kim J-S 2020 Order improvement of surface nanopatterns via substrate rocking under ion bombardment: experiments and nonlinear models *Phys. Rev.* B **102** 045421

[229] Kim J, Yoon S M, Jo S, Seo J and Kim J 2018 Nanopatterning by ion beam sputtering in unconventional formats *J. Phys.: Condens. Matter* **30** 274004

[230] Li J, Yang G, Bradley R M, Liu Y, Frost F and Hong Y 2021 Enhancing the quality of self-organized nanoripples by Ar-ion bombardment of a bilayer system *Nanotechnology* **32** 385301

[231] Ziberi B, Cornejo M, Frost F and Rauschenbach B 2009 Highly ordered nanopatterns on Ge and Si surfaces by ion beam sputtering *J. Phys.: Condens. Matter* **21** 224003

[232] Ziberi B, Frost F, Höche T and Rauschenbach B 2005 Ripple pattern formation on silicon surfaces by low-energy ion-beam erosion: experiment and theory *Phys. Rev.* B **72** 235310

[233] Ziberi B, Frost F, Tartz M, Neumann H and Rauschenbach B 2008 Ripple rotation, pattern transitions, and long range ordered dots on silicon by ion beam erosion *Appl. Phys. Lett.* **92** 063102

[234] Zhang K, Bobes O and Hofsäss H 2014 Designing self-organized nanopatterns on Si by ion irradiation and metal co-deposition *Nanotechnology* **25** 085301

[235] Karmakar P and Satpati B 2016 The influence of projectile ion induced chemistry on surface pattern formation *J. Appl. Phys.* **120** 025301
[236] Mukherjee J, Bhowmik D, Mukherjee M, Satpati B and Karmakar P 2020 Alternating silicon oxy-nitride and silicon oxide stripe formation by nitric oxide (NO^+) ion implantation *J. Appl. Phys.* **127** 145302
[237] Mukherjee J, Bhowmik D, Bhattacharyya G, Satpati B and Karmakar P 2022 Spatially varying chemical phase formation on silicon nano ripple by low energy mixed ions bombardment *J. Phys.: Condens. Matter* **34** 135001